Preprint
UCRL-JC-145878

Indirect-Drive Non-Cryogenic Double-Shell Ignition Targets for the National Ignition Facility: Design and Analysis

P. Amendt, J. Colvin, R.E. Tipton, D. Hinkel, M.J. Edwards, O.L. Landen, J.D. Ramshaw, L.J. Suter, R.G. Watt

U.S. Department of Energy

Lawrence
Livermore
National
Laboratory

This article was submitted to
43rd Annual Meeting of the Division of Plasma Physics, Long Beach, California, October 29 – November 2, 2001

October 15, 2001

Approved for public release; further dissemination unlimited

DISCLAIMER

This document was prepared as an account of work sponsored by an agency of the United States Government. Neither the United States Government nor the University of California nor any of their employees, makes any warranty, express or implied, or assumes any legal liability or responsibility for the accuracy, completeness, or usefulness of any information, apparatus, product, or process disclosed, or represents that its use would not infringe privately owned rights. Reference herein to any specific commercial product, process, or service by trade name, trademark, manufacturer, or otherwise, does not necessarily constitute or imply its endorsement, recommendation, or favoring by the United States Government or the University of California. The views and opinions of authors expressed herein do not necessarily state or reflect those of the United States Government or the University of California, and shall not be used for advertising or product endorsement purposes.

This is a preprint of a paper intended for publication in a journal or proceedings. Since changes may be made before publication, this preprint is made available with the understanding that it will not be cited or reproduced without the permission of the author.

This report has been reproduced directly from the best available copy.

Available electronically at http://www.doe.gov/bridge

Available for a processing fee to U.S. Department of Energy
and its contractors in paper from
U.S. Department of Energy
Office of Scientific and Technical Information
P.O. Box 62
Oak Ridge, TN 37831-0062
Telephone: (865) 576-8401
Facsimile: (865) 576-5728
E-mail: reports@adonis.osti.gov

Available for the sale to the public from
U.S. Department of Commerce
National Technical Information Service
5285 Port Royal Road
Springfield, VA 22161
Telephone: (800) 553-6847
Facsimile: (703) 605-6900
E-mail: orders@ntis.fedworld.gov
Online ordering: http://www.ntis.gov/ordering.htm

OR

Lawrence Livermore National Laboratory
Technical Information Department's Digital Library
http://www.llnl.gov/tid/Library.html

Indirect-drive non-cryogenic double-shell ignition targets for the National Ignition Facility: Design and analysis

Peter Amendt, J. Colvin, R.E. Tipton, D. Hinkel, M.J. Edwards, O.L. Landen, J.D. Ramshaw, L.J. Suter, and R.G. Watt*

University of California, Lawrence Livermore National Laboratory, Livermore, California 94551
**University of California, Los Alamos National Laboratory, Los Alamos, New Mexico 87545*

Abstract

The central goal of the National Ignition Facility (NIF) is demonstration of controlled thermonuclear ignition. The mainline ignition target is a low-Z, single-shell cryogenic capsule designed to have weakly nonlinear Rayleigh-Taylor growth of surface perturbations. Double-shell targets are an alternative design concept that avoids the complexity of cryogenic preparation but has greater physics uncertainties associated with performance-degrading mix. A typical double-shell design involves a high-Z inner capsule filled with DT gas and supported within a low-Z ablator shell. The largest source of uncertainty for this target is the degree of highly evolved nonlinear mix on the inner surface of the high-Z shell. High Atwood numbers and feed-through of strong outer surface perturbation growth to the inner surface promote high levels of instability. The main challenge of the double-shell target designs is controlling the resulting nonlinear mix to levels that allow ignition to occur.

Design and analysis of a suite of indirect-drive NIF double-shell targets with hohlraum temperatures of 200 eV and 250 eV are presented. Analysis of these targets includes assessment of two-dimensional radiation asymmetry as well as nonlinear mix. Two-dimensional integrated hohlraum simulations indicate that the x-ray illumination can be adjusted to provide adequate symmetry control in hohlraums specially designed to have high laser-coupling efficiency [Suter *et al.*, Phys. Plasmas **5**, 2092 (2000)]. These simulations also reveal the need to diagnose and control localized 10-15 keV x-ray emission from the high-Z hohlraum wall because of strong absorption by the high-Z inner shell. Preliminary estimates of the degree of laser backscatter from an assortment of laser-plasma interactions suggest comparatively benign hohlraum conditions. Application of a variety of nonlinear mix models and phenomenological tools, including buoyancy-drag models, multimode simulations and fall-line optimization, indicates a possibility of achieving ignition, i.e., fusion yields greater than 1 MJ. Planned experiments on the Omega laser to test current understanding of high-energy radiation flux asymmetry and mix-induced yield degradation in double-shell targets are described.

I. Introduction

The National Ignition Facility[1] (NIF) is scheduled to demonstrate thermonuclear ignition after 2008 when 1.8 MJ of laser energy at 3ω will be available. The baseline ignition target consists of a hohlraum-driven single-shell capsule consisting of a low-Z ablator over a DT ice layer and is filled with DT gas [See Fig. (1a)].[2] The target specifications require that the capsule be kept near the triple-point of DT (18.3°K) and the RMS ice roughness be below one micron. Current techniques to control the ice roughness consist of β-layering[3] and auxiliary IR heating[4]. The required ice smoothness has been recently demonstrated,[5] but preparing and fielding a cryogenic ignition target remains a complex procedure. In addition the baseline design requires that the capsule be driven by a four-step high-contrast (50-to-1) laser pulse-shape with 500 TW peak power. The ignition mode is via formation of a hot spot at capsule center and propagation of a thermonuclear burn wave to the remaining DT fuel. One-dimensional (1D) radiation-hydrodynamics simulations predict 15 MJ of undegraded yield and a capsule absorbed energy of 150 kJ.[6]

The four principal challenges of achieving ignition with the baseline design are ensuring: (1) adequate DT ice smoothness, (2) precision shock-timing to within ±100 ps,[7] (3) acceptable time-averaged and –dependent low-order mode hohlraum radiation flux uniformity,[8] and (4) robust laser-target coupling[9]. To meet these goals an exhaustive experimental campaign, begun on the Nova laser and continuing with the University of Rochester's Omega laser[10], has been in place. The aim of this decade-long campaign is to directly address these aforementioned technical issues, to reduce the physics uncertainties and to maximize our confidence in achieving ignition on the NIF.

Given the complexity of cryogenic preparation, an interesting option is to reconsider double-shells as an additional vehicle for demonstrating and exploring ignition on the NIF. Double-shells consist of a low-Z ablator (outer) shell that collisionally impacts a high-Z (inner) shell filled with high-density DT gas at room temperature [See Figs. (1b-d)]. The outer shell acts as an efficient absorber of hohlraum-generated x rays which magnifies and transfers the acquired energy density upon spherical convergence and subsequent collision with the inner shell. The main function of the high-Z inner shell is to greatly limit radiative losses from the igniting fuel and to provide added inertia for delaying fuel disassembly. The ignition mechanism for double-shells is simpler than in the cryogenic single-shell case, requiring only volumetric ignition of the fuel. Thus, careful shock sequencing is unnecessary because the fuel adiabat is not constrained to a low value and simpler laser pulse shapes may be entertained. For example, rather than having peak laser power occur at late-time when the hohlraum has filled with potentially problematic high-density plasma, more benign hohlraum plasma conditions are possible if the laser power is arranged to peak at early time. In this way, plasma-induced backscatter losses may be less of an issue for indirect-drive double-shells. Additional advantages of a double-shell ignition target include: (1) a lower peak implosion speed for ignition, (2) relaxed symmetry requirements as a result of the relatively low characteristic fuel convergence (≈ 10), and (3) lower ignition temperatures (≈ 4 keV) compared to hot-spot ignition ($\approx 10\,\mathrm{keV}$)[11].

The concept of ignition double-shells has its origin in the 1970's when high-gain "Apollo" targets were explored at LLNL.[12]These cryogenic double-shell designs absorbed 800 kJ of energy and yielded 313 MJ according to calculations that excluded the effects of mix. In 1979 a few double-shells were fielded on the Shiva laser but with generally low neutron yields ($< 10^7$). In the 1980's it became recognized that a significant design challenge of ignition double-shell targets was controlling the highly evolved nonlinear mix on the inner surface of the high-Z shell to levels that would avoid inner shell breakup. For this reason, LLNL abandoned double-shells as a viable path to high-gain ignition, but LANL maintained an interest and conducted some double-shell experiments on the Nova laser in the 1990's. The LANL double-shell targets consisted of glass inner shells filled with DT gas and a CH outer ablator. However, these targets performed poorly without exception, giving measured over predicted clean neutron yields (YoC) only on the order of 1%. At the time, it was conjectured that intrinsic flux asymmetry and significant laser power imbalances were responsible for the marginal performance on Nova. To test this hypothesis similar double-shell targets, though fielded within a tetrahedral hohlraum instead of a cylindrical hohlraum, were shot on the Omega laser. These targets performed as earlier with no appreciable improvement. However, a new type of double-shell target was tested which was designed to allow imaging of the pusher by thinning the glass micro-balloon and over-coating with CH. One-dimensional clean behavior, i.e., YoC's approaching unity, was observed for these so-called "imaging" double-shell capsules.[13] These targets were repeated in cylindrical hohlraums on Omega in November 2000 and showed continued good performance. In addition, double-shells using only pure CH were also fielded for the first time and showed similarly high YoC behavior. However, the pure glass inner-shell double-shell targets still failed to provide significant YoC performance.

One of the reasons offered for the poor performance of the standard double-shell targets to date is the role of Au hohlraum M-shell (2-4 keV) flux asymmetry.[14] While the lasers are turned on a significant fraction of the hohlraum radiation fraction ($\approx 6\%$) resides in an M-shell component originating from the laser spots. The concern is that appreciable M-shell non-uniformity on the inner shell may seed the growth of surface perturbations that may disrupt the inner-shell integrity at late time. To test this conjecture LANL has recently fielded a direct-drive version of the standard double-shell targets for which M-shell radiation asymmetry is nonexistent. At the time of writing the results are inconclusive and the contribution of M-shell asymmetry to degraded performance in hohlraum-driven standard double-shells remains an open question.

An essential requirement for any promising NIF double-shell ignition target design is that the double-shell database with its aforementioned mix of successes and failures be sufficiently understood. Such an understanding will necessitate further experiments on Omega for development and validation. This paper builds on a previous LANL double-shell ignition design[14] for the NIF by seeking increased margin to the potentially destructive mix of high-Z pusher material and hot DT fuel. A useful figure-of-merit in this regard is the fuel-pusher fall-line which gauges the potential for mix to degrade an implosion. Very simply, a fall-line is the (straight-line) trajectory that material from the fuel-pusher interface moving at peak implosion speed would follow toward the origin if deceleration near the end of the implosion were absent. A hypothetical limit on the spatial extent of mixed material is given by the fall-line trajectory. That is to say, the mixed material is expected to remain above the fall-line on account of causality. Therefore, an implosion with a delayed fall-line trajectory is seen as advantageous from the standpoint of reducing the effects of mix. We adopt this strategy in optimizing the NIF double-shell target design. An important trade-off between yield and fall-line behavior is found requiring greater capsule absorbed energy to recover a modest amount of yield. Thus, two-dimensional (2D) integrated hohlraum simulations with LASNEX[15] are required to ascertain the energetics and provide absolute design constraints. At the same time we obtain information on hohlraum flux asymmetry control and hohlraum plasma conditions.

The main results of this paper can be summarized as follows. In the process of optimizing double-shell fall-line behavior we find that smaller and thicker inner shells, i.e., having lower aspect ratio η, give significantly improved robustness to mix. We also obtain that the constant (in time) drive-temperature profiles (T_R=200 and 250 eV) rather than the constant 300 TW power case considered by LANL (giving hohlraum temperatures of nearly 300 eV) are associated with improved fall-line behavior. In addition, the laser power history required for a constant T_R is beneficial from the standpoint of minimizing the effects of plasma-mediated backscatter: peak power occurs very early in the pulse before the hohlraum has filled with "tenth-critical density" ($0.1n_c$) plasma. Symmetry tuning of the double-shell target underscores the importance of controlling energetic x-ray (10-15 keV L-shell) flux asymmetry. Significant L-shell emission below the laser spots is preferentially absorbed by the high-Z inner shell near the pole (or hohlraum symmetry axis). Considerable displacement of the NIF inner and outer cones by nearly 1 mm is required to effect satisfactory symmetry tuning. The simulated hohlraums are found to be quite efficient compared to the standard NIF cryogenic point design, giving capsule absorbed energies as high as 30% of the input laser energy. Consequently, some justification for assuming high capsule absorbed energies in the 1D scoping studies which result in improved fall-line behavior is provided. We next apply a suite of state-of-the–art mix calculations to the 250 eV design to quantify the improved robustness to mix as suggested by fall-line arguments. Multimode simulations used to gauge the degree of feed-through of outer surface perturbations to the inner surface of the high-Z shell indicate minimal performance degradation largely as a result of the lower aspect ratio shells used. Next we apply *K-L* sub-grid turbulence mix modeling to estimate the amount of yield degradation from potentially destructive short-wavelength perturbations growing on the inner surface of the inner shell. For an arguably realistic set of model parameters we find that the optimized 250 eV double-shell design still ignites in marked contrast to the former 300 eV design. As a further check on inner-surface short-wavelength perturbation growth we apply the Ramshaw model[16] for nonlinear mixing. Again, our 250 eV double-shell design readily ignites according to this test.

Whether the level of nonlinear mix is sufficient to thwart ignition of NIF double-shells is a key concern confronting the viability of these targets. To date we have applied a suite of modern turbulence models to gauge target robustness to short-wavelength turbulence but with the caveat that these models are phenomenological at their core. That is to say, input parameters such as bubble drag and buoyancy coefficients are required for implementation of these models. Past investigations using the linear electric motor (LEM)[17] and ongoing implosion campaigns on the Omega laser have strived to constrain these coefficients to the maximum extent possible. Thus, confidence in a double-shell ignition design depends critically on the ability of experiments to benchmark and validate various turbulence models beforehand. In this vein, experiments are proposed on Omega to simulate some of the features of our NIF double-shell ignition designs as a means of testing our understanding of mix.

The paper is organized as follows. In Section 2 we present some analytical preliminaries and introduce the 200 eV and 250 eV ignition designs based on fall-line optimization criteria. In Section 3 we describe our 2D integrated hohlraum simulation results and the consequences for symmetry, energetics and hohlraum plasma conditions. In Section 4 we present quantitative predictions on yield degradation from mix in the intermediate- and short-wavelength regimes based on modern turbulence mix calculations. In Section 5 we propose some campaigns on Omega to begin to address some of the outstanding issues regarding double-shell performance. We summarize in Section 6.

II. Double-shell analysis and design

a) Analytic preliminaries

A useful starting point for understanding double-shell behavior is to undertake some simple analysis. First we address the question of optimum momentum transfer from the outer shell to the inner shell. We start with the rocket equation

$$M_1 \frac{dv_1}{dt} = v_E \frac{dM_1}{dt} \ , \quad (1)$$

where M_1 is the mass of the outer shell, $v_1(<0)$ is the implosion speed and $v_E(>0)$ is the exhaust speed. In the thinshell approximation we can write:[18]

$$M_1(t) = M_1(0) + 4\pi \int_0^t dt' r^2(t') \cdot \dot{m}(t') \ , \quad (2)$$

where $\dot{m}(<0)$ is the areal mass ablation rate and r is the spherical radial coordinate. Combining Eqs. (1,2) we find

$$v_1(t) = v_E \ln\left[1 + \frac{4\pi}{M_1(0)} \int_0^t dt' \dot{m}(t') \cdot r^2(t')\right] , \quad (3)$$

where v_E is assumed constant. We next form the product of Eqs. (2,3) to obtain the momentum of the outer shell. Maximizing this expression for the shell momentum gives

$$\frac{4\pi}{M_1(0)} \int_0^{t_o} dt' \ r^2(t') \cdot \dot{m}(t') = \frac{1}{e} - 1 \ . \quad (4)$$

Thus, maximum momentum of the outer shell is attained at t_o when nearly two-thirds of the shell has ablated away. This simple exercise provides guidance for optimizing the spacing of the two shells and is corroborated by radiation-hydrodynamics simulations.

We next address the degree of velocity multiplication imparted to the inner shell from the outer shell upon collision. If the outer shell of mass M_1 has speed v_{1i} before and v_{1f} after the collision, and if the inner shell of mass M_2 has momentum v_{2f} after the collision, then energy and momentum conservation give:

$$\frac{v_{2f}}{v_{1f}}=\frac{2M_1/M_2}{1+M_1/M_2} \ . \quad (5)$$

Thus, a factor-of-two velocity enhancement is possible in the limit of large outer shell to inner shell mass ratio. For the double-shell designs that we describe in detail later the initial mass ratio is on the order of ten, but use of Eq. (4) lowers this to nearly three at the instant of collision. Thus, a velocity enhancement of 50% is possible in the limit of no energy dissipation.

However, radiation-hydrodynamics simulations suggest that the degree of velocity multiplication for NIF double-shells is quite minimal, typically less than 10%. This feature points to the presence of significant energy dissipation at the instant of collision which we can analytically estimate. Defining Q as the fraction of outer shell kinetic energy that is dissipated as heat during the shell collision, we apply energy conservation and assume $v_{1f}=v_{2f}$ to find:

$$Q=\frac{1}{1+M_1/M_2} \ . \quad (6)$$

Thus, nearly 25% of the outer shell kinetic energy is dissipated by collision for $M_1/M_2=3$.

As we remarked in the Introduction, peak implosion speeds of ignition double-shells are significantly less than cryogenic single-shell capsules which depend on hot-spot ignition. To illuminate this difference we follow Lindl[6] and invoke energy conservation at the instant of ignition onset:

$$P_w+P_\alpha+P_r+P_e=2.3\times10^{15}\frac{\rho T(v_{imp}/10^7)}{r}+8\times10^{16}\rho^2\left\langle\frac{\sigma v_{imp}}{10^{-17}}\right\rangle F_\alpha - 3\times10^{16}\rho^2 T^{1/2}\cdot\varepsilon-8\times10^{12}\frac{T^{7/2}}{r^2}\ [W/cm^3] =0 \ . \quad (7)$$

Here, P_w is the rate of compressional work done on the fuel, P_α is the thermonuclear heating rate of the fuel by α-particle deposition, P_r is the rate of radiative loss from the fuel, P_e is the rate of conductive losses from the fuel, T is the temperature, ρ is the fuel density, and ε is an effective albedo of the high-Z shell. One distinguishing feature of double-shell ignition is the (anticipated) reduced radiative losses from the fuel due to the high-Z shell containing the DT fuel. This is illustrated in Fig. 2 where Eq. (7) is plotted with ($\varepsilon=1$) and without ($\varepsilon=0$) radiative losses for a peak implosion speed $v_{\text{imp}}=20$ cm/μs. Also overlaid on this plot is a typical trajectory through T-[ρr] space of an ignition double-shell driven at 200 eV. Without radiative trapping, ignition is not possible at low v_{imp} because of the clear inaccessibility of the high temperature and high areal density domain. This scenario is representative of a low-Z (cryogenic) pusher where radiative equilibrium in the fuel is not established. By contrast the high-Z pusher of a double-shell traps the radiation in the fuel and promotes radiative equilibrium with the inner surface of the pusher. As shown in Fig. (2) the double-shell trajectory traverses both of the $\varepsilon=1$ (shaded) regions to ignite at a temperature of several keV and an areal density of 0.4 g/cm^2. At higher implosion speeds, e.g., $v_{imp}=30$ cm/μs, the shaded $\varepsilon=1$ regions coalesce to allow ignition of a cryogenic single-shell capsule [Fig. 1a].[6]

b) 1D double-shell designs

Our starting point is the 1D ignition design of Harris and Varnum[13] as shown in Fig. (1b). This design requires 300 TW of laser power delivered over 6 ns to give a hohlraum temperature T_R of nearly 300 eV and a capsule yield of nearly 2.4 MJ. Here we pursue an alternative design approach which emphasizes robustness to deleterious mixing of high-Z pusher material and hot DT fuel. The figure-of-merit we will use is a so-called "fall-line" of the implosion trajectory of the fuel-pusher interface. The idea of a fall-line analysis is as follows. The contamination of the fuel is causally limited to the extent that high-Z material cannot overtake the position the interface would have if it continued to move inward to the origin ($r=1$) at its peak velocity. The tangent line to the interface trajectory at the time of deceleration onset, i.e., peak v_{imp}, defines a fall-line which will intercept $r=0$ at some later time. In order to minimize the effects of mix one legislates that the fall-line intercept the origin after peak burn by as much a margin as possible. Forming the difference between the instant of peak burn and time at which the fall-line reaches the origin, normalized to the FWHM burn-width, defines the fall-line delay parameter $\Delta\tau$. The philosophy of this work is to minimize $\Delta\tau$ at any cost, including the sacrifice of significant yield if necessary. Our intention is the demonstration of thermonuclear ignition - not high gain - which requires aggressive control of damaging mix.

The direction we choose to pursue for minimizing $\Delta\tau$ is through use of constant hohlraum drive-temperatures and higher capsule absorbed energies. A constant T_R is beneficial from the standpoint of requesting peak laser power very early in time before the hohlraum has appreciably filled with high-Z plasma from wall blow-off. In addition, damage initiation of the laser glass may be reduced with use of such a pulse-shape [See Section III]. We will explore hohlraum drive temperatures of 200 eV and 250 eV, the former being easily accessible on the Omega laser for experimental scoping studies. Improved fall-line behavior is also correlated with increased capsule absorbed energy as we now show analytically. Applying energy conservation to the fuel and pusher as the fuel is adiabatically compressed gives for the pusher velocity:

$$v_2(r) = -v_{imp}\sqrt{1-\frac{1}{\beta}\left(\frac{r_0^2}{r^2}-1\right)}, \quad (7)$$

where v_{imp} is the pusher velocity at the the instant of deceleration onset t_0, r_0 is the radius of fuel-pusher interface at t_0. Here, the parameter β is defined as:

$$\beta = \frac{M_2 v_{imp}^2}{4\pi P_s r_f^3}\left(\frac{r_0}{r_f}\right)^2 = 1-\left(\frac{r_f}{r_0}\right)^2, \quad (8)$$

where P_s is the fuel stagnation pressure and r_f is the minimum radius attained by the fuel at t_f. The time $\delta t=t_1-t_0$ required to reach stagnation ($v_2=0$) is obtained from integration of Eq. (7):

$$\delta t = \frac{r_0}{v_{imp}}\cdot\frac{\beta}{1+\beta}. \quad (9)$$

Good fall-line behavior is associated with δt small compared to the fall-line time $r_0/v_{\rm imp}$ which is tantamount to small β. From Eq. (8) a trajectory of the fuel-pusher interface that can reach peak implosion speed $v_{\rm imp}$ just before fuel stagnation will minimize β and ensure favorable fall-line behavior. This condition of reaching $v_{\rm imp}$ at higher fuel pressure can be met most directly by accessing higher capsule absorbed energies.

We now develop some scaling law relations to facilitate consideration of different capsule absorbed energies. Let the parameter s denote the capsule absorbed energy. For the constant drive conditions of interest the flux remains constant so that $r^2 t \propto s$. From Eq. (4) with $\dot{m} \approx T_R^3$ and $M_1 \propto r^3$, we have $r \propto t$. We thus obtain the following scaling relations:

$$r \to r \cdot s^{1/3},\ t \to t \cdot s^{1/3},\ v \to v,\ P \to P \cdot s^{2/3}, \quad (10)$$

where P is the power.

Our 500 kJ 200 eV double-shell design is depicted in Fig. (1c). Aside from the overall 60% larger scale of this target compared to the 350 kJ former target [Fig. (1b)], we emphasize some important design differences. First, the (inner) shell aspect-ratio η is considerably larger than in the former design for two reasons: (1) to facilitate target fabrication with respect to containment of the high fuel fill, and (2) to reduce feed-through $[\approx \exp(-\ell/\eta)]$ of outer surface perturbations with Legendre mode number ℓ. Second, we have dispensed with Cu-dopant in the beryllium ablator in order to maintain a high mass-ablation rate and keep the peak implosion velocity above the critical value of 19 cm/μs. Third, we increased the DT fuel fill by 30% to provide more yield margin. The design strategy was to vary the ablator thickness for a given inner shell thickness and radius until optimal fall-line behavior was achieved. Figures (3a-b) illustrate the result of this procedure for capsule absorbed energies of 500 kJ and 750 kJ. The tradeoff between acceptable fall-line behavior and yield is very evident: nearly a factor-of-two in thermonuclear yield is sacrificed in order to accommodate negative values of $\Delta\tau$. Another feature of note is that the fall-line behavior for the 750 kJ case [Fig. (3b)] is improved beyond the near factor-of-two improvement in yield as well.

The 670 kJ 250 eV design is schematically shown in Fig. (1d). Again, the distinguishing features of this target are the markedly lower aspect-ratio inner shell, the reduced Cu-dopant concentration in the outer shell (0.3 at.%) compared to the former design [Fig. (1b)], the modestly higher fuel fill, and the larger ratio of shell radii (≈ 3). The clean yield for this target is 4.1 MJ and $\Delta\tau \approx -1$. The relatively thicker and smaller inner shell in this design is intended to provide improved fall-line behavior. Figures (4a-b) show the yield and fall-line behavior for very similar capsules at 500 kJ and 750 kJ of absorbed energy. A main distinction with Figs. (3a-b) is the relative robustness of larger inner-shell designs driven at 250 eV. We now see that the $\Delta_{\rm fuel}$=–20% design has far more favorable fall-line behavior than the corresponding 200 eV versions. This feature allows access to considerably higher yield while controlling the potential for damaging mix. A caveat is that the improvement in fall-line behavior comes at the expense of relatively higher aspect-ratio inner-shells which may promote stronger feed-through of perturbations. Comparing the $\Delta_{\rm fuel}$=-40% targets in the 200 eV and 250 eV designs shows overall that the higher drive case is characterized by modestly better fall-line behavior but somewhat lower yields. To regain the higher yields while maintaining good fall-line behavior in the 250 eV case may require stronger consideration of the $\Delta_{\rm fuel}$=–20% targets.

We have not looked at 300 eV versions of the above double-shell targets to date. However, the laser power requirements and the higher risk of damage initiation to the laser glass slabs possibly will not make this type of target an attractive double-shell option.

III. Energetics and symmetry

Having established the merit of high capsule absorbed energy for achieving double-shell ignition, we now turn our attention to the practicality of fielding such targets in a NIF hohlraum. To address this question, we must perform 2D integrated hohlraum simulations for assessing the energetic requirements and tuning the flux asymmetry to acceptable levels for ignition.

a. 2D Analysis of 200 eV hohlraum

A 200 eV hohlraum enclosing the previously described 500 kJ double-shell capsule is shown schematically in Fig. (5). Two cones of rays from each side are incident on the interior of a hohlraum made from a "cocktail" mixture of high-Z elements (26% U, 18% Pb, 18% Ta, 19% Dy, 19% Nd) for reducing wall losses and thereby improving laser-target coupling.[9] The laser-entrance-holes (LEHs) are 60% and the hohlraum is filled with a 1 mg/cm^3 equimolar mixture of He-H to aid in symmetry control. Beam-phasing between the outer and inner cones is not invoked. The laser power history is shown in Fig. (6) and corresponds to 1.6 MJ of laser energy. Note that the hohlraum is calculated to be quite efficient by historical standards, exceeding 30%. Further improvement in target coupling is possible with use of even smaller LEHs due to the relatively large scale of the hohlraum ("scale" 1.6) under consideration and the fixed spot size of the rays at best focus ($\approx 250\mu m$ radius). A polyimide window for containing the hohlraum gasfill has not been included in this first generation simulation study but is not expected to materially affect our conclusions.

A key concern for any NIF pulse-shape is the initiation of damage to the final optics assembly from localized absorption and heating of blue light near glass surface imperfections. The damage integral takes the form:[9]

$$Damage = 1.1 \times \int_0^t \frac{I(s)}{\sqrt{t-s}} ds \ , \quad (11)$$

where I is the laser intensity [GW/cm^2], t and s are in nanoseconds, and the coefficient of 1.1 normalizes the damage for a 3ns Gaussian-equivalent pulse-shape which is a convenient metric of comparison. Figure (7) shows the laser glass damage-initiation integral calculated for the 3ω pulse-shape shown in Fig. (6). From a damage threshold standpoint the 200 eV drive laser pulse-shape is rather benign, giving less than half the indicated NIF damage specification.

We have succeeded in obtaining ignition of our 200 eV 500 kJ double-shell target according to our integrated hohlraum simulations. The thermonuclear yield is almost 2 MJ which is to be compared with the 1D yield of 3.2 MJ. The symmetry of the implosion is clearly not ideal and tends toward the "pancaked" direction, i.e., the 2nd Legendre coefficient of the imploded fuel-pusher interface is negative. Figures (8a-b) shows the 2nd and 4th Legendre coefficient of ablation pressure asymmetry for both shells versus time; higher resolvable even-mode radiation asymmetries (ℓ=6, 8) do not appear to have a significant effect in the simulations. Figure (8a) verifies that the outer shell lower mode ($\ell = 2, 4$) ablation pressure asymmetry is remarkably good up to the time of shell collision with the time-integrated ablation pressure asymmetry less than 2% for both P_2 and P_4. However, Fig. (8b) indicates a rather different situation for the inner shell ablation pressure asymmetry. The time-integrated ablation pressure asymmetry up to the time of shell interaction is nearly 12% for P_2 and 17% for P_4, both of which add in concert to cause pancaked implosions and abbreviated thermonuclear burn. Ordinarily, such a large level of flux asymmetry would preclude the possibility of ignition. The exception in our case is because the ablation pressure on the inner shell is only 2-3% of the outer shell ablation pressure before shell collision. However, this level of asymmetry is still sufficient to modestly degrade the yield.

On closer inspection of this source of flux asymmetry on the inner shell, one finds that a significant fraction ($\approx 10\%$) of the radiation density in the volume between the two shells resides in high-energy x rays, i.e., 8-15 keV. The source of this L-shell radiation seen in the simulations is the high-Z hohlraum blow-off material intercepting the laser rays near the LEHs. In order to satisfactorily tune away this L-shell flux asymmetry component both inner and outer cones were displaced inward by over a millimeter compared to the baseline cryogenic hohlraum designs. This phenomenon of L-shell flux asymmetry is unique to indirectly-driven double-shells because of the presence of a highly absorbing high-Z inner shell. The following exercise underscores this point further. If we replace the single-shell cryogenic target shown in Fig. (1a) with the former double-shell design [Fig. (1b)] in the NIF point-design hohlraum,[2] the double-shell fails convincingly to ignite. However, to our surprise the double-shell readily ignites in 1D for an applied drive extracted from the same point-design hohlraum. Besides confirming the robustness of double-shell ignition, this exercise clearly distinguishes the effect of hohlraum L-shell asymmetry on low- and high-Z targets.

As we have mentioned the effect of L-shell asymmetry was partly controlled by moving the cones inward, i.e., considerably shortening the hohlraum. The use of higher gas densities in the hohlraum and implementing beam phasing between the outer and inner cones are possible methods for mitigating this novel source of flux asymmetry.

We have also started to consider the effect of plasma-mediated laser backscatter in the 200 eV hohlraum with the aid of the Laser-plasma Interaction Postprocessor[19] (LIP). LIP obtains the calculated flow speeds, temperatures and densities along a laser raypath from a radiation-hydrodynamics code to estimate linear growth-factors of stimulated Brillouin backscatter (SBS) and stimulated Raman backscatter (SRS). We initially ran LIP on our 200 eV hohlraum design where the inner cone foci were situated 0.2 cm inside of the LEH. Large SBS growth was found to occur in the He-H gas just outside of the LEH. To ameliorate this SBS growth we moved the inner cone foci 0.2 cm outside of the LEH and found much improved plasma conditions. As shown in Fig. (9a) the linear SBS gain-length is a maximum near peak laser power, reaching ≈ 18 which nearly matches the value predicted[6] for the inner-cone on the NIF point-design at peak power (≈ 20). For both hohlraums most of the gain occurs in the low-Z gas, although well inside the LEH for the case of the point-design. Much of this relatively high SBS found in the 200 eV design is due to the relatively low temperature (≈ 3keV) of the gas outside the LEH and the long plasma pathlength (≈ 0.7 cm) despite relatively low electron density ($n_e/n_c \approx 0.04$) and peak intensity ($\approx 10^{15}$ W/cm^2). In the outer cones the peak SBS is calculated to reach only ≈ 13 linear gain-lengths compared to nearly 18 for the point design.

Figure (9b) shows the simulated SRS streaks for the inner cone of the 200 eV design. The peak SRS gain-length is only ≈ 12, well below the predicted value of nearly 22 for the point design[6]. Much of this improvement is due to the strong dependence of SRS gain-length on electron density $[\approx (n_e/n_c)^{5/3}]$, where n_e/n_c is nearly a factor-of-three lower for our 200 eV hohlraum. For the outer cone SRS gain-lengths of only ≈ 7 are approached compared to ≈ 10 for the point design. Overall, the indicated backscatter in our 200 eV hohlraum design appears to be manageable with the flexibility for further reduction if needed.

b. Integrated hohlraum analysis of 250 eV design

We carry through the same analysis for the 250 eV double-shell target design [Fig. (1d)]. The hohlraum used to drive this 670 kJ target is illustrated in Fig. (10). Overall the hohlraum is about $(4/3)^{1/3}$ times smaller in dimension than the 200 eV hohlraum driving our 500 kJ target [Fig. (5)]. The required laser power history is shown in Fig. (11) and the corresponding damage-initiation integral is illustrated in Fig. (12). The total laser energy is 2.5 MJ with a peak power of nearly 600 TW but the NIF damage limit is still comfortably avoided. With this damage margin the requested energy at 3ω appears possible despite being higher than the nominal 1.8 MJ. A NIF 2ω option would provide further damage margin and allow even higher laser energies.[9] To relax further the laser requirements a longer risetime of the laser pulse-shape could be implemented without jeopardizing ignition. The resulting lower intensity translates into lower levels of plasma-mediated backscatter. A lower intensity would also reduce damage from the well-known effect of accumulating nonlinear phase retardation over an optical path length ("B-integral"):[20] $B = (3\omega / c) \cdot \int ds \cdot n_I$ where n_I is the nonlinear refractive index contribution. Experience has shown that B needs to be less than about 2 radians to avoid noise ripple growth. We find B=1.8 for the laser power history shown in Fig. (11), leaving once again little margin for avoiding laser glass damage.

The target yield from this 2D simulation is 2.8 MJ which compares favorably with the 1D yield of 4.1 MJ. Again, flux asymmetry is conjectured to be the dominant degradation mechanism as in the case of the 200 eV design. Figure (13a) shows that the ablation pressure asymmetry on the outer shell is benign just as in the 200 eV case, cf. Fig. (8a). Although the time-integrated ablation pressure asymmetry on the inner shell as shown in Fig. (13b) appears much improved over the 200 eV case, cf. Fig. (8b), the asymmetry is magnified by the increased level of 10-15 keV flux reaching the inner shell for the 250 eV hohlraum. For example, the time-integrated ablation-pressure asymmetry up to shell collision is about three-times less ($P_2 \approx 5\%, P_4 \approx 1\%$), but the ratio of peak ablation pressure is about three-times greater than for the 200 eV design. Thus, the effects of flux asymmetry are magnified by the increased level of 10-15 keV x rays reaching the inner shell for the higher temperature hohlraum (250 eV). Increasing the Cu-dopant in the Be outer shell for the 250 eV target would reduce the flux reaching the inner surface, but not without incurring a significant penalty in mass ablation rate. Higher mode radiation asymmetries ($\ell = 6,8$) appear to be tolerably low for this hohlraum because of robust radiation transport smoothing[8] ($\approx \ell^{-2.5}$) and the large ratio of hohlraum radius to inner shell radius (≈ 20).

As in the 200 eV design, further improvement in tuning lowest-order mode asymmetry is required. Although the yield degradation in the designs is only about 30% from flux asymmetry alone, higher-mode perturbations such as from feed-through can be superimposed on the low-order distortions to the point of thwarting ignition altogether. For this reason symmetry optimization is an essential component of overall mix control. Beyond the $\ell = 2-8$ even modes considered in this section, tolerances to low-order odd modes arising from target imperfections, e.g., shell non-concentricity ($\ell = 1$) and laser power imbalances, must be established.

IV. Intermediate-wavelength perturbations

We have just assessed some of the possible effects of low-order mode radiation-driven perturbations on target performance via integrated hohlraum simulations. We now turn our attention to an intermediate regime of perturbation wavelengths that can adversely impact target performance. An important concern for double-shell stability is the feed-through of outer-surface perturbations on the inner shell to the inner surface. At the time of shell collision, an impulsive-like acceleration will be delivered to the outer surface of the inner shell promoting Richtmyer-Meshkov instability [RM]. Subsequent shocks propagating across this interface will transmit the amplified perturbations to the inner surface according to the feed-through expression: $FT = \exp(-\ell / \eta)$. Therefore, shells with a large aspect-ratio promote the largest instability growth and possible shell disruption. We can analytically estimate the most dangerous mode number and its growth as follows. The Rayleigh-Taylor [RT] growth factor for an inner surface perturbation at deceleration onset scales as $\approx \exp(\sqrt{2\ell})$, where the conduction scale-length is ignored and the deceleration distance is taken to be the final fuel radius. Forming the product of this growth-factor and the feed-through factor above, and then solving for the maximum growth GF, gives

$$GF \approx e^{\eta/2} \quad at \quad \ell = \eta^2 / 2. \quad (12)$$

Thus, with $\eta \approx 6-7$ for our double-shell target designs, maximum growth occurs for $\ell \approx 20-25$. This range of mode numbers is amenable to direct numerical simulation (DNS) which we have performed with CALE[21] using a (Au-like) measured glass surface power spectrum to initialize the perturbations [Fig. 14(a)]. Figure (14b) shows fuel-pusher interface and ion temperature contours 150 ps after peak burn for the 250 eV design [Fig. (1d)] using $\ell_{\max} = 32$. Simulations with higher mode-number cutoff ($\ell_{\max} = 96$) show very similar results with a yield degradation of only several percent. At the instant of peak burn the perturbations are barely perceptible which is attributable to the optimized fall-line behavior, low aspect-ratio inner shell, and realistically smooth surface spectrum.

V. Short-wavelength perturbations

Until now we have considered resolvable perturbations and their calculable effect on target performance. Unfortunately, we are not currently able to make DNS predictions much beyond ℓ=100, and we must resort to more established (and controversial) phenomenological methods for estimating the contribution to mix from unresolved short-wavelength modes. In the absence of ablative and density-gradient scale length stabilization, the short wavelength modes will nonlinearly saturate after reaching an amplitude on the order of their wavelength. Thus, very short-wavelength modes will quickly reach saturation and the peak of the accumulating perturbation energy spectrum will shift to longer wavelengths with time. A dominant perturbation at low mode number ($\ell < 100$) often emerges to determine the overall integrity of the shell.[22] A full spectrum of modes is required to describe this process deterministically, but the computational requirements are generally prohibitive for the relevant regime of large Reynolds number (*Re*>1000). The spectrum of growing modes is bounded above by those modes that are viscously damped: $\ell > 2\pi \cdot Re \cong 10^4$, where ν is the kinematic viscosity of the Au shell. In addition, the dissipation of energy for large *Re* occurs over small spatial scales or "eddies" ($\approx r_f \cdot Re^{-3/4}$) with characteristic size on the order of a hundred nanometers or less for ignition double-shells. Describing such small-scale structure *ab initio* with DNS techniques is not currently practical and we resort to other techniques.

a. *K-L* turbulence modeling

The *K-L* sub-grid turbulence mix model in CALE has been exercised for our 250 eV double-shell design [Fig. (1d)]. Here, *K* refers to the turbulent or eddy kinetic energy per mass that resides in modes which are computationally unresolved and have not yet thermalized or dissipated their kinetic energy into heat. *K* can be defined in this manner even when the system has not reached a statistical steady-state normally referred to as turbulence. The second parameter of the model *L* is the eddy scale length which is used in place of the more familiar parameter:[22] $\varepsilon = C_D K^{3/2} / L$ where C_D is the bubble drag coefficient. The *K-L* representation is more convenient from the standpoint of specifying and remembering initial conditions, i.e., initial surface finish, which are essential for properly describing the RM instability. The *K-L* equations comprise a system of coupled nonlinear equations to which must be added the diffusion equations for species concentration and energy. This system of equations is then solved in conjunction with a standard hydro code, e.g., CALE, to assess the evolution of mix and its effect on target performance. Figure (15) shows the fuel-pusher interface trajectory and the intrusion of high-Z Au into the fuel volume after minimum radius for our 250 eV design. According to this simulation our double-shell target ignites to produce over 1 MJ of yield; by contrast, the former design [Fig. (1b)] fails to ignite. The difference is a direct result of the improved fall-line behavior and of reduced perturbation feed-through. We must emphasize that the *K-L* model is phenomenological at its core, and, as such, relies on a suite of parameters for implementation. Although our adopted set of modeling parameters arguably enjoys experimental support, other choices not compatible with ignition are also possible. Ongoing experiments on the Omega laser and past analysis of LEM data are currently being used to further constrain these parameters and improve the predictive capability of the *K-L* mix model.

b. Ramshaw nonlinear mix model

Another buoyancy-drag model closely related to the *K-L* treatment is due to Ramshaw.[16] This model obtains a second-order ordinary differential equation for the mix width h for an arbitrary acceleration history $a(t)$:

$$\dot{\lambda}\cdot\ddot{h}+\frac{1}{2}\dot{\lambda}\cdot\dot{h}+2\pi c\left|\dot{h}\right|\dot{h}-2\pi Aah=0 \quad , (12)$$

where λ is the perturbation wavelength, $A=(\rho_2-\rho_1)/(\rho_1+\rho_1)$ is the Atwood number, ρ_1 and ρ_2 are the densities of the adjacent fluids, and b and c are constants constrained by the asymptotic behavior of the RT and RM instabilities. Equation (12) reproduces the known linear and nonlinear behavior for the RT and RM instabilities. Further work has generalized Eq. (12) to include the effects of shear and compression. The Ramshaw model has been recently implemented in LASNEX for mix studies. Figure (15) shows the results of the Ramshaw model applied to our 250 eV double-shell design. The fundamental input quantity is the ratio of initial perturbation amplitude to the perturbation wavelength. Figure (16) provides the maximum initial value of A_ℓ / λ_ℓ versus ℓ that the capsule can tolerate while still providing a yield of 1 MJ [top curve]. As a basis of comparison we include the glass spectrum from Fig. (14a) [bottom curve]. Clearly, a large margin of initial perturbation amplitude is allowed according to the model. However, the Ramshaw model does not include perturbation feed-through and explicit mode-coupling which may erase much of the margin.

The effect of perturbation feed-through can be estimated as follows. Upon shell collision an outer surface perturbation on the inner shell will grow according to the (ideal) RM growth-rate: $A_n(t)=A_n(0)\cdot k_n\cdot\Delta r$, where k_n is the perturbation wavenumber and Δr is the distance the interface has travelled before a 2nd shock arrives to propagate the amplified perturbation to the inner surface [See Section VI]. The feed-through factor is nearly exponential for $\ell>10$, i.e., $FT\approx\exp(-\ell/\eta)$, but spherical effects become important at smaller values of ℓ, requiring the following modification: $FT\approx1/[(1+1/\eta)^{\ell}-(1+1/\eta)^{-\ell-1}]$. We form the product of the above RM growth-rate and the feed-through factor, taking Δr as the radius of the shell for an upper-limit, and apply the result to the surface spectrum in Fig. (16) as shown [dotted line].

We can now estimate an upper limit for the effects of mode-coupling by collapsing all of the perturbation amplitude, including feed-through, into a single mode and then initializing the Ramshaw model with use of this rms amplitude. Figure (16) shows the result of this procedure and the remaining margin for achieving 1 MJ yield [dotted-dashed curve]. Over the entire range of mode numbers shown the Ramshaw mix model suggests that ignition of the 250 eV double-shell target is possible. The caveat for this analysis is again the underlying phenomenological basis of the model through a reliance on a set of parameters requiring experimental validation.

c. Fall-line analysis

We have gone to considerable length to optimize fall-line behavior as a necessary condition for target robustness. In this section we quantify the effect of a given fall-line delay on target performance in terms of a phenomenological penetration fraction γ.

For RT dominated perturbation growth the fall-line analysis can be shown to have an intuitively close connection with nonlinear RT behavior. Youngs has shown that a similarity solution with length scale proportional to gt^2 describes the late time evolution of the mixing layer where g is the acceleration of the interface.[22] Subsequent studies have established that the mix width evolution in the nonlinear regime can be well described by the relation:

$$h_i=\alpha_i Ag\cdot(t-t_o)^2, \quad (13)$$

where i=1,2 labels the fluid being penetrated, α_1 (α_2) is the growth coefficient for spikes (bubbles), and $\alpha_1 > \alpha_2$. Experiments show that α_2 is relatively insensitive to Atwood number, assuming values in the range of 0.04-0.07.[17] Spike penetration of the fuel on the other hand show more variation with A: $\alpha_1 \cong \alpha_2 \cdot (1+A)$ for $A<0.8$. Equation (13) can be related to a fall-line analysis. Near minimum volume of the imploding fuel the trajectory of the fuel-pusher interface can be approximated as

$$r(t) \cong L - v_{imp} \cdot (t-t_o) + \frac{v_{imp} \cdot (t-t_o)^2}{2(t_f - t_o)}. \quad (14)$$

Forming the difference between Eq. (14) and the fall-line trajectory $r_{fall} = L - v_{imp}(t-t_o)$ gives for the fall-line difference Δr_{fall}:

$$\Delta r_{fall}(t) = \frac{v_{imp}(t-t_o)^2}{2(t_f - t_o)}. \quad (15)$$

Comparing Eqs. (13,15) suggests the natural introduction of a time-independent penetration fraction γ of the fuel by pusher material. That is to say, we have established a theoretical basis for representing the spatial evolution of fuel-pusher mixing in terms of a (constant) fraction of the distance between of the interface and the fall-line. In reality, the presence of RM instability and a time-varying Atwood number will complicate this simple picture somewhat, but the property of a one-parameter (γ) description of the mix process is nonetheless appealing.

We have analyzed the 250 eV double-shell design for yield performance versus fall-line penetration fraction γ. Figure (17) offers a comparison of this design with the former design [Fig. 1b)], showing significantly more tolerance to high-Z pusher penetration of the fuel. Note that the effect of feed-through is not explicity included in a fall-line analysis although an implicit dependence through γ can be expected. Thus, for the same fall-line behavior a double-shell target with more benign feed-through will command a smaller penetration fraction than for a high aspect-ratio inner shell as in the former design [Fig. (1b)]. Figure (17) shows that the 250 eV design can tolerate as much as 40% bubble penetration fraction and still give over 1MJ of yield. The increased margin is a result of more energy absorbed by the capsule and improved fall-line behavior as evidenced in Fig. (17) by the slower decrease in yield with increasing penetration fraction. By comparison the NIF cryogenic capsule can tolerate a mix penetration depth of 29% for a half-yield of 7.5 MJ.[6]

VI. Double-shell database and future directions

The fall-line figure-of-merit has played a prominent role in our exploration of robust double-shell ignition designs. An important question to address is the possibility of a fall-line interpretation of the Nova and Omega double-shell database. As we noted in the Introduction the performance of double-shells to date has been spectacularly successful or disappointing depending on the type of inner-shell fielded. In Fig. (18) we show the neutronic YoC behavior of three generic types of double-shell that have been shot over the past two years on Omega versus fall-line parameter $\Delta\tau$. An interesting correlation is seen between fall-line behavior and performance. The best performing targets had large (negative) $\Delta\tau$ while the underachieving targets had significantly positive $\Delta\tau$ without exception. This plot is intended only to demonstrate that the current Omega double-shell database is consistent with a fall-line interpretation; other hypotheses for the (all) glass inner-shell target performance such as target fabrication irregularities or M-shell flux asymmetry are not invalidated. The M-shell hypothesis for target degradation has been previously proposed as a leading candidate for the historically low performance of the standard double-shell target.[13] For this reason, the recent direct-drive campaign with double-shells was meant to test their performance in the complete absence of M-shell asymmetry. Unfortunately, issues regarding target preparation and laser-imprinting have compromised the results to the point that a definitive judgment on the role of M-shell asymmetry is not yet in hand.

Given that M-shell effects may still be key to the success of indirectly-driven double-shell performance a prudent course is to consider experimental methods for *in situ* measurements of M-shell flux and asymmetry near the center of the hohlraum. Figure (19) shows a proposed experimental setup using a double-shell target geometry to directly measure the properties of M-shell flux. A large low-Z outer shell absorbs almost all of the thermal x-ray flux but allows over 80% of 2-4 keV radiation to be transmitted to the inner-shell which consists of a glass micro-balloon overcoated with 25 μm of CH. The glass readily absorbs the transmitted x rays but its radial expansion is heavily tamped by the overlying CH. Thus, the glass is forced to expand inward and standard x-ray backlighting techniques can directly track the trajectory of this M-shell driven implosion. A large outer shell is chosen in order to delay the collision with the inner shell until the preheat-driven implosion has advanced sufficiently for diagnostic detection. We estimate that a 10% P_2 flux asymmetry in 2-4 keV radiation will translate into nearly -10 μm P_2 distortion of the glass by the time of half-convergence. By tracking the trajectory of the imploding glass direct information on the level of M-shell flux and asymmetry can be obtained.

Beyond the effect of asymmetry, M-shell radiation can affect double-shell performance in another important respect. All of the high YoC targets shown in Fig. (18) are influenced to a considerable extent by volume absorption and heating of the inner-shell due to M-shell preheat. The inner-shell thus behaves as an exploding pusher to an appreciable degree, promoting early and robust neutron production at arrival of the first shock at the expense of neutron production from the subsequent stagnation phase of the implosion. By constrast the standard double-shells do not behave in this mode, producing the vast majority (>90%) of their yield during fuel stagnation and thereby assuming an increased risk of mix-induced degradation. The current challenge for the double-shell effort is to field an "ignition-like" target on Omega which emulates many (but obviously not all) of the properties of the ignition target described earlier while still giving good YoC behavior. Figure (20) displays some of the salient aspects of the 250 eV ignition target in terms of shock behavior that could prove helpful in designing the next generation double-shell experiment on Omega. There are two important features in Fig. (20) worth pointing out. First, two principal shocks drive the implosion. Second, we note that the second shock originates at intermediate time from a rarefaction fan reaching the ablation front. This shock collides with a reflection shock originating from passage of the outer surface of the inner-shell by the first shock. We have found that favorable fall-line behavior coincides well with the second shock collision occurring near the inner surface of the outer shell. Thus, we refer to ignition-like behavior when the implosion is dominated by two principal shocks as just described with a relative timing such that the second shock collides with a reflected shock near the inner edge of the outer shell. To capture such ignition-like properties we propose that a variant of the pure CH double-shells successfully fielded on Omega be modifed by doping the outer shell to reduce the M-shell preheat of the inner shell. Designs are in progress to optimize this design and to adapt standard core-imaging techniques, e.g., Ar-doping of the fuel, for aggressive diagnosis of double-shell implosion symmetry.

VII. Summary

Using modern mix calculations, integrated hohlraum simulations and fall-line optimization we have begun to assess the viability of double-shell ignition on the NIF. Together these methods form the basis for our optimism that the prospects for achieving double-shell ignition have improved. The path to double-shell ignition will require a dedicated experimental commitment with the Omega laser to benchmark our understanding of mix and asymmetry. With regard to mix the calculations done to date reveal no adverse surprises, but in lieu of their phenomenological nature such predictions must be considered as tentative at best. Continuing experimental efforts aimed at constraining the relevant model parameters will likely lead to an improved predictive capability and a benefit for double-shell research. Rather than focusing on a particular mix model to validate a double-shell ignition design we have emphasized the fall-line figure-of-merit as a physically appealing tool for minimizing mix. Additional margin to mix may be required depending on the evolving status of modern mix calculations. Such techniques may include the introduction of a low-Z mix-mitigation layer on the inner surface of the high-Z inner shell. For example, seamless fabrication of the inner shell will likely require a low-Z mandrel to initiate the process of shell construction. Ordinarily, this mandrel is designed to be removable by leaching through an outer layer of shell material. However, an advantage for double-shells may be to leave the mandrel intact, serving as a partial barrier between high-Z pusher and low-Z fuel. Preliminary calculations using a 20 micron thick layer of Be inside the Au/Cu shell are promising and show unchanged fall-line behavior and only modest deterioration in yield with such a low-Z buffering layer. Use of denser inner shell materials in double-shell simulations, e.g., a Pt/Ir alloy (80/20), also suggest improved performance giving higher yield and more fall-line delay.

Acknowledgments

We are grateful to O. Jones, D. Rowley and G. Dimonte for useful discussions. This work was performed under the auspices of the U.S. Department of Energy by the Lawrence Livermore National Laboratory under Contract No. W-7405-Eng-48.

Figure Captions

Fig. 1a-d: Schematic diagrams of (a) NIF point-design cryogenic capsule, (b) 300 TW NIF double-shell ignition design, (c) 200 eV NIF 500 kJ double-shell ignition design, and (d) 250 eV NIF 670 kJ double-shell ignition design.

Fig. 2: Fuel gain (G) in areal density (ρr) and temperature (T) space for peak implosion speed of 20 cm/μs with (ε=1) and without (ε=0) radiative losses. Central fuel trajectory for simulated double-shell implosion is represented by solid line. Dark grey areas represent accessible region with radiative loss in fuel (ε=1); accessible region in absence of radiative loss (ε=0) is indicated by dark grey region *and* unshaded region (lower right).

Fig. 3a-b: Normalized fall-line parameter $\Delta\tau$ and simulated one-dimensional yield versus changes in inner-shell thickness Δ_{Au} and fuel radii Δ_{fuel} driven at 200 eV for (a) 500 kJ design and (b) 750 kJ design. Indicated changes are relative to former design [Fig. (1b)] scaled in dimension by (a) $4^{1/3}$ and (b) $6^{1/3}$.

Fig. 4a-b: Normalized fall-line parameter $\Delta\tau$ and simulated one-dimensional yield versus changes in inner-shell thickness Δ_{Au} and fuel radii Δ_{fuel} driven at 250 eV for (a) 500 kJ design and (b) 750 kJ design driven. Indicated changes are relative to former design [Fig. (1b)] scaled in dimension by (a) $(2.25)^{1/3}$ and (b) $(3.4)^{1/3}$.

This work was performed under the auspices of the U.S. Department of Energy by the University of California, Lawrence Livermore National Laboratory under Contract No. W-7405-Eng-48.

Fig. 5: Schematic of hohlraum geometry for 200 eV 500kJ double-shell design.

Fig. 6: Simulated laser power history for 200 eV hohlraum [Fig. (5)] driving 500 kJ double-shell target.

Fig. 7: Calculated damage initiation integral for 200 eV hohlraum with indicated NIF damage threshold.

Fig. 8a-b: Normalized second- and fourth-Legendre coefficient of ablation pressure asymmetry history in (a) outer shell and (b) inner shell for 200 eV 500 kJ double-shell target.

Fig. 9a-b: (a) Simulated SBS gain in inner cone versus time and wavelength shift for 200 eV hohlraum [Fig. (5)]. (b) Simulated SRS gain in inner cone versus time and wavelength for 200 eV hohlraum.

Fig. 10: Schematic of hohlraum geometry for 250 eV 670kJ double-shell design.

Fig. 11: Simulated laser power history for 250 eV hohlraum [Fig. (10)] driving 670 kJ double-shell target.

Fig. 12: Calculated damage initiation integral for 250 eV hohlraum with indicated NIF damage threshold.

Fig. 13a-b: Normalized second- and fourth-Legendre coefficient of ablation pressure asymmetry history in (a) outer shell and (b) inner shell for 250 eV 670 kJ double-shell target.

Fig. 14a-b: (a) Measured surface power spectrum of glass capsule fielded on Omega laser; (b) simulated ion temperatures (upper frame) and zoning mesh (lower frame) for 250 eV 670 kJ double-shell target +150 ps after peak thermonuclear burn using surface spectrum from (a). Heavy black line marks location of simulated fuel-pusher interface.

Fig. 15: Simulated mix fraction of Au versus time with overlayed fuel-pusher interface using CALE with KL mix model for 250 eV 670 kJ double-shell target.

Fig. 16: Ratio of amplitude to wavelength versus Legendre mode number for measured glass spectrum (lower curve), measured glass spectrum with calculated feed-through amplification (dotted line), rms glass spectrum including feed-through (dot-dashed line), and calculated 1 MJ threshold value based on Ramshaw mix model (upper curve) applied to 250 eV 670 kJ double-shell target design.

Fig. 17: One-dimensional simulated yield versus bubble penetration fraction for 250 eV 670 kJ design (solid line) and former 300 TW design [Fig. (1b)].

Fig. 18: Measured neutron yield over simulated clean (no mix) yield versus normalized fall-line parameter $\Delta\tau$ for indicated Omega LANL directly-driven and cylindrical hohlraum-driven targets. CH targets are pure plastic inner and outer shell double-shells filled with DD; glass targets have pure glass inner shell with 1.8% Br-doped CH outer shell and DT fill; imaging targets have glass inner shell overcoated with CH and undoped outer CH shell; high-yield version of imaging targets have higher DD fuel fill and thinner outer shell.

Fig. 19: Schematic of experimental design on Omega for M-shell asymmetry experiment.

Fig. 20: Simulated logarithmic derivative of density versus time and Lagrange coordinate (integrated mass) for 250 eV 670 kJ double-shell design.

References

---

[1] J.A. Paisner *et al.*, Laser Focus World 30, 75 (1994).

[2] S.W. Haan, S.M. Pollaine, J.D. Lindl *et al.*, Phys. Plasmas **2**, 2480 (1995).

[3] J.K. Hoffer et al, Nucl. Fusion Research 1992, Vol. **3**, p. 443, IAEA, Vienna (1993); J. Sanchez and W.H. Giedt, Fusion Tech. **36**, 346 (1999).

[4] G.W. Collins *et al.*, J. Vac. Sci. Technol. A **14** (5), 2897 (1996).

[5] J. Sater *et al.*, Fusion Tech. **36**, 229 (1999).

[6] J.D. Lindl, *Inertial Confinement Fusion* (Springer-Verlag, New York, 1998), p. 55.

[7] D.H. Munro *et al.*, Phys. Plasmas **8**, 2245 (2001).

[8] S.M. Pollaine *et al.*, Phys. Plasmas **8**, 2357 (2001).

[9] L.J. Suter *et al.*, Phys. Plasmas **7**, 2092 (2000).

[10] T.R. Boehly *et al.*, Opt. Commun. **133**, 495 (1997).

[11] S.A. Colgate and A.G. Petschek, "Minimum conditions for the ignition of fusion", LA-UR-88-1268 (1988).

[12] J.D. Lindl, "Apollo targets for Nova and Kr-F driven reactors", Laser Program Annual Report (1978), LLNL, Livermore, Ca, UCRL-50055-78, pp. 2-77 – 2-88 (unpublished).

[13] W.S. Varnum et al., Phys. Rev. Lett. **81**, 5153 (2000).

[14] D.B. Harris and W.S. Varnum, Bull. Am. Phys. Soc., **41**, 1479 (1996).

[15] G.B. Zimmerman and W.L. Kruer, Comments Plasma Phys. Control. Fusion **2**, 51 (1975).

[16] J.D. Ramshaw, Phys. Rev. E **58**(5), 5834 (1998).

[17] G. Dimonte and M. Schneider, Phys. Rev. E **54**, 3740 (1996); G. Dimonte, Phys. Plasmas **6**(5),2009 (1999).

[18] P. Amendt, A.I. Shestakov, O.L. Landen *et al.*, Phys. Plasmas **8**(6), 2908 (2001).

[19] L.V. Powers, R.L. Berger, R.L. Kauffman *et al.*, Phys. Plasmas **2**(6), 2473 (1995).

[20] J.H. Campbell *et al.*, Inertial Confinement Fusion **9**(2), 111 (1999)

[21] R.E. Tipton, D.J. Steinburg, and Y. Tomita, Japan Soc. Mech. Eng. Int. J. Ser. II **35**, 67 (1992).

[22] D.L. Youngs, Physica D **12**, 32 (1984).

[23] C.G. Speziale, Annu. Rev. Fluid Mech. **23**, 107 (1991).

Fig. 1a

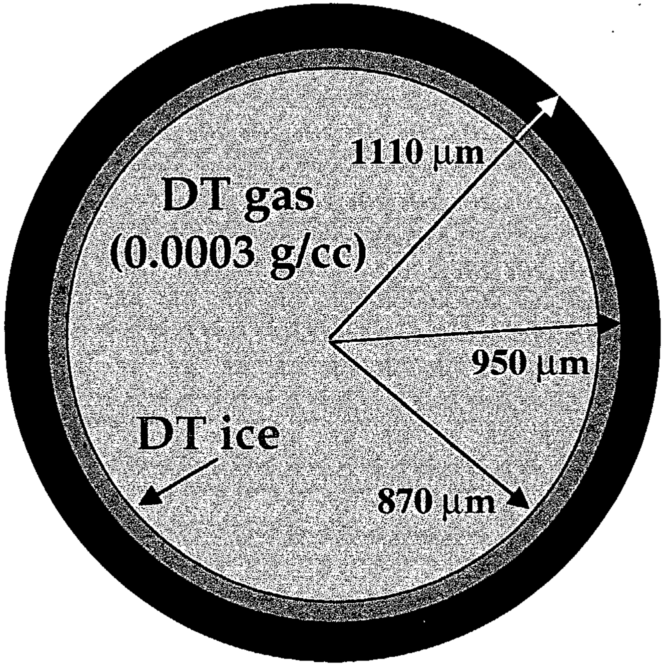
1110 μm
DT gas
(0.0003 g/cc)
950 μm
DT ice
870 μm

0.25% Br-doped CH

Fig. 1b

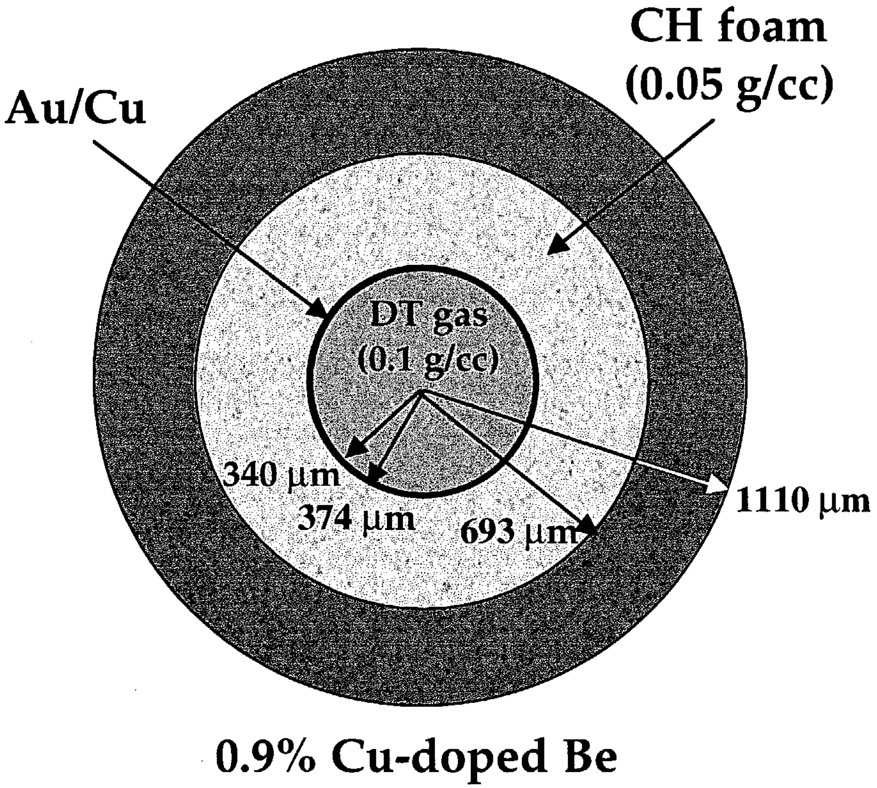
CH foam
(0.05 g/cc)
Au/Cu
DT gas
(0.1 g/cc)
340 μm
374 μm
693 μm
1110 μm
0.9% Cu-doped Be

Fig. 1c

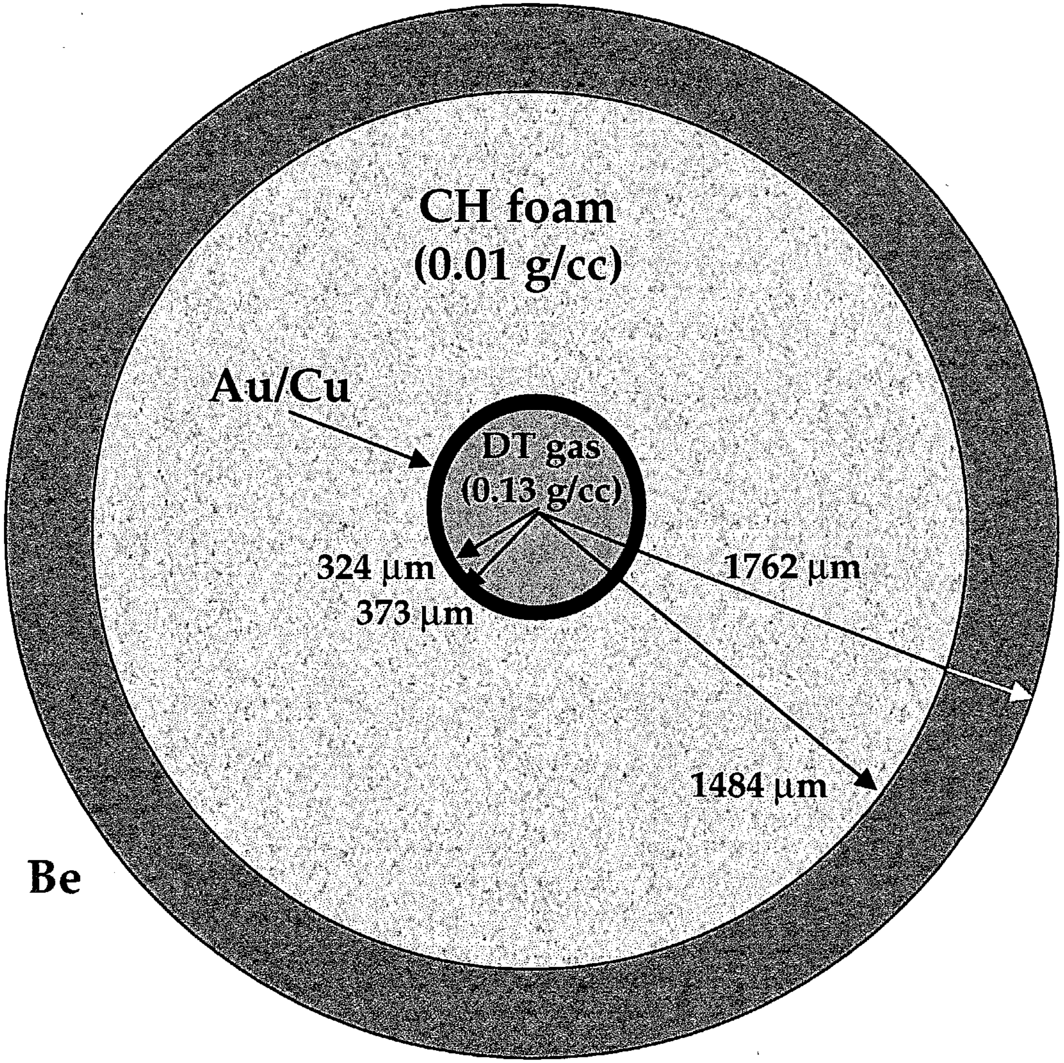
CH foam
(0.01 g/cc)
Au/Cu
DT gas
(0.13 g/cc)
324 µm
373 µm
1762 µm
1484 µm
Be

Fig. 1d

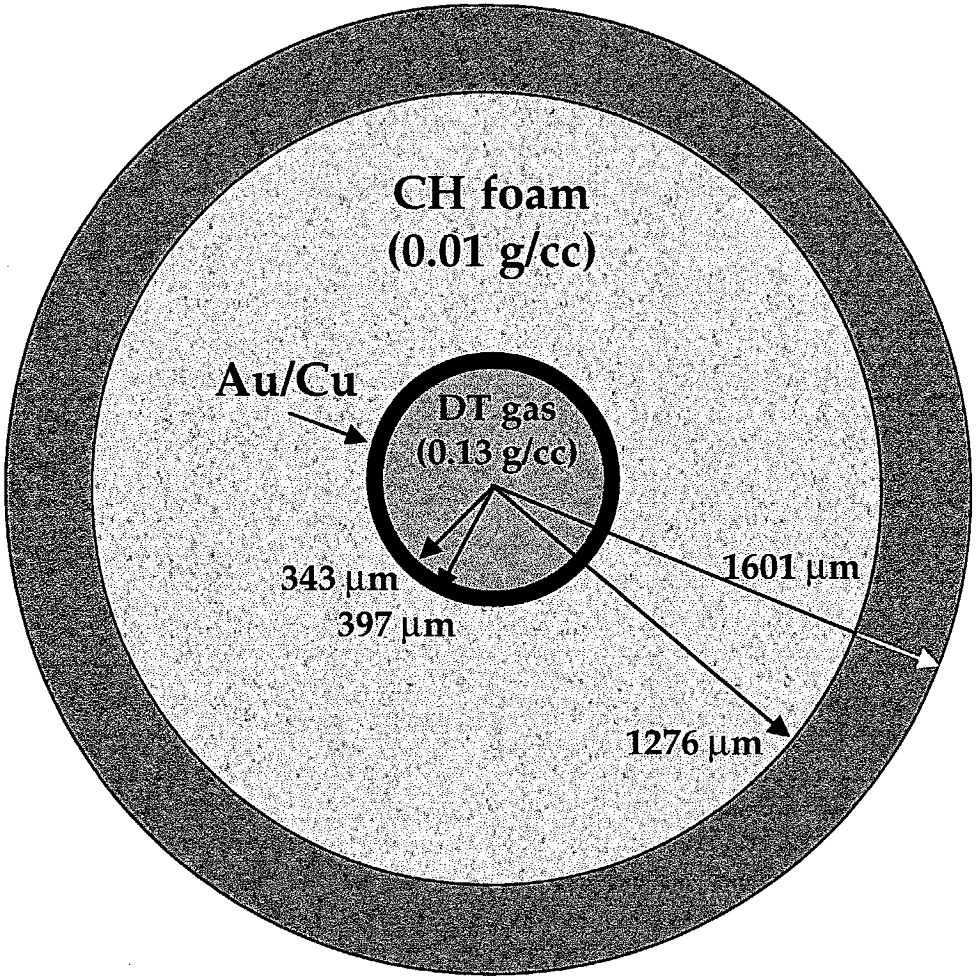
CH foam
(0.01 g/cc)
Au/Cu
DT gas
(0.13 g/cc)
343 µm
397 µm
1601 µm
1276 µm

0.3% Cu-doped Be

Fig. 2

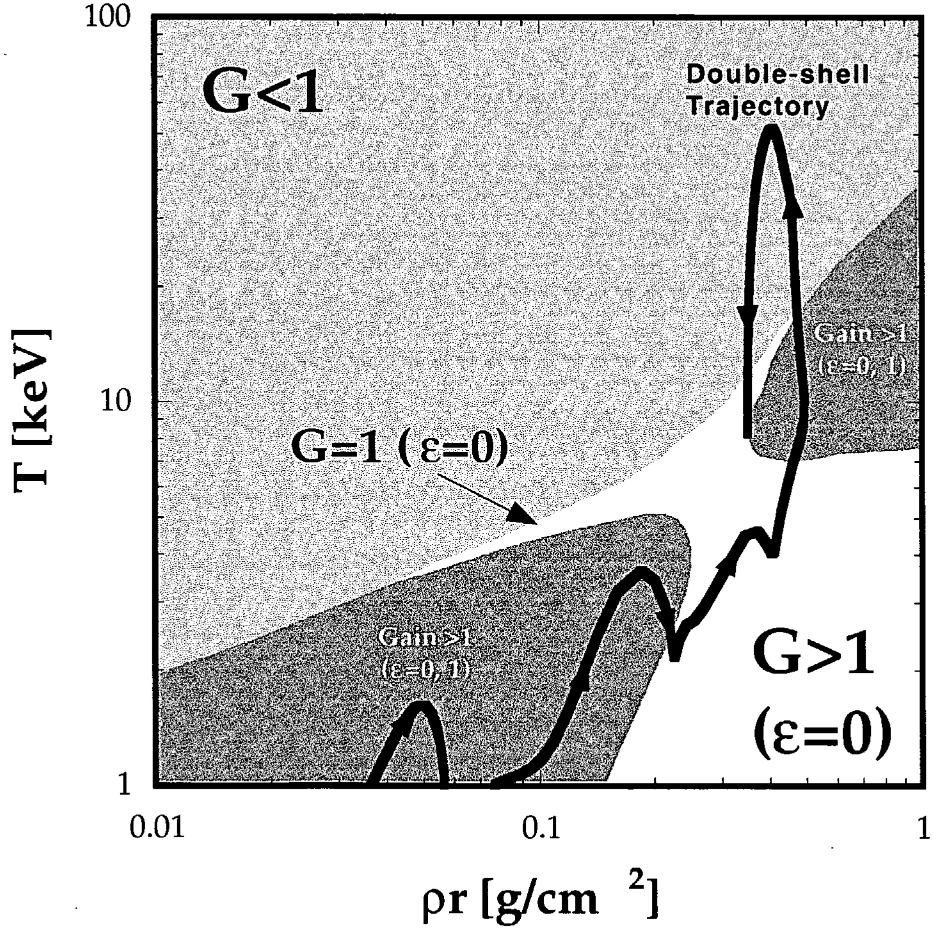
100
10
1
0.01
0.1
1
T [keV]
ρr [g/cm 2]
G<1
Double-shell Trajectory
Gain>1 (ε=0, 1)
G=1 (ε=0)
Gain>1 (ε=0, 1)
G>1 (ε=0)

Fig. 3a

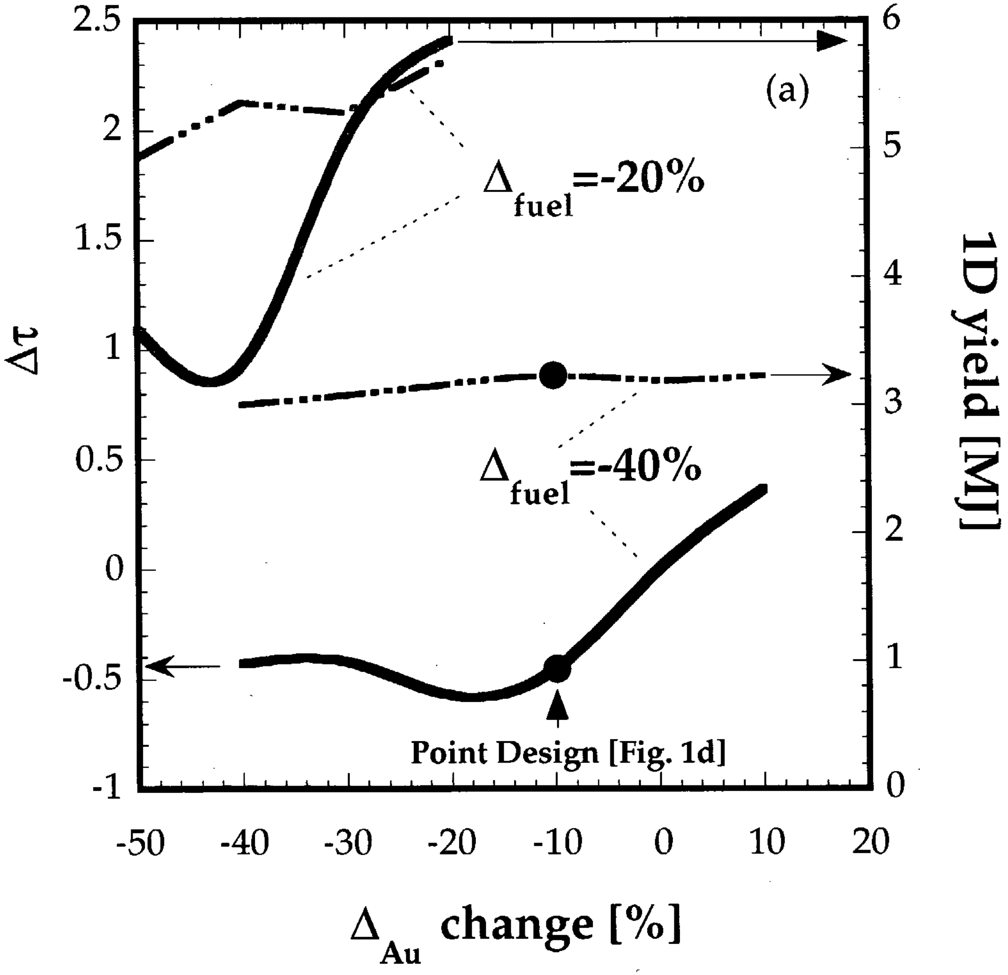

(a)
Δ_{fuel}=-20%
Δ_{fuel}=-40%
Point Design [Fig. 1d]
Δτ
2.5
2
1.5
1
0.5
0
-0.5
-1
1D yield [MJ]
6
5
4
3
2
1
0
-50
-40
-30
-20
-10
0
10
20
Δ_{Au} change [%]

Fig. 3b

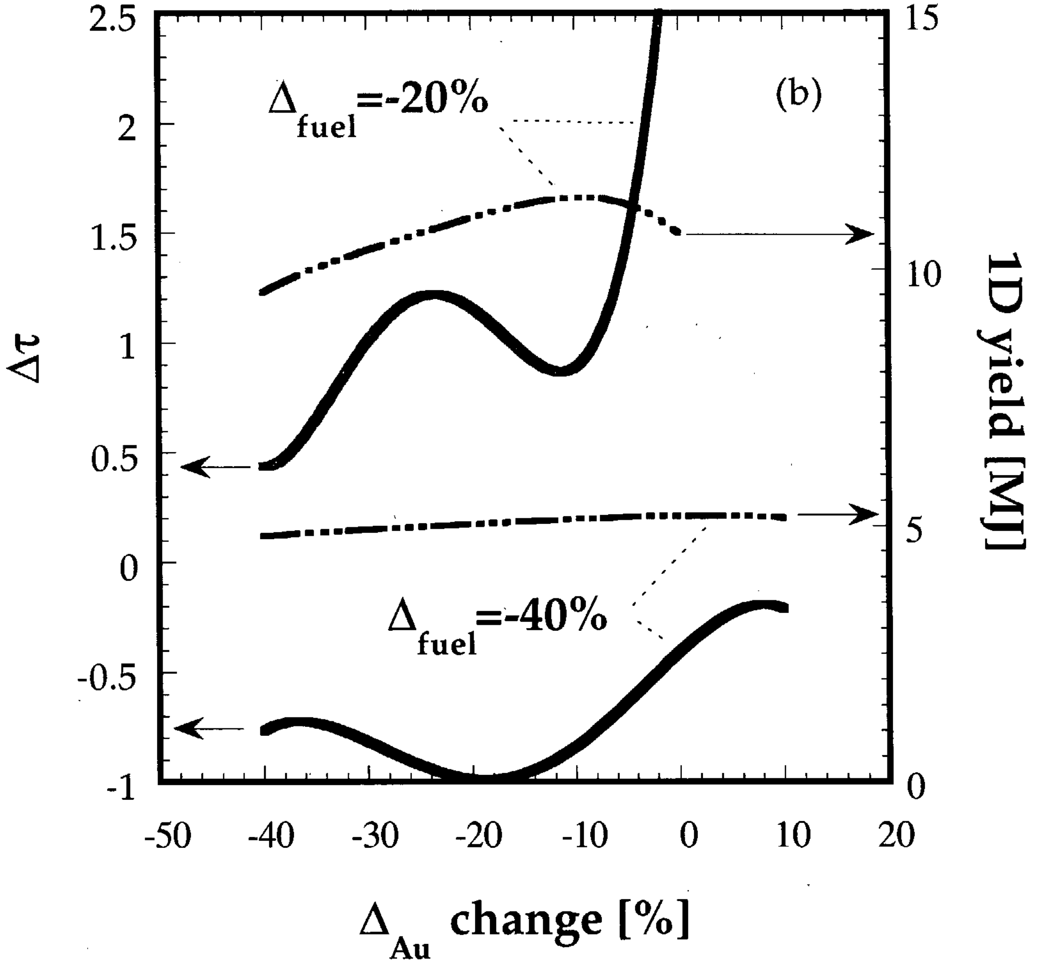

(b)
Δ_{fuel}=-20%
Δ_{fuel}=-40%
$\Delta\tau$
1D yield [MJ]
Δ_{Au} change [%]
2.5
2
1.5
1
0.5
0
-0.5
-1
15
10
5
0
-50
-40
-30
-20
-10
0
10
20

Fig. 4a

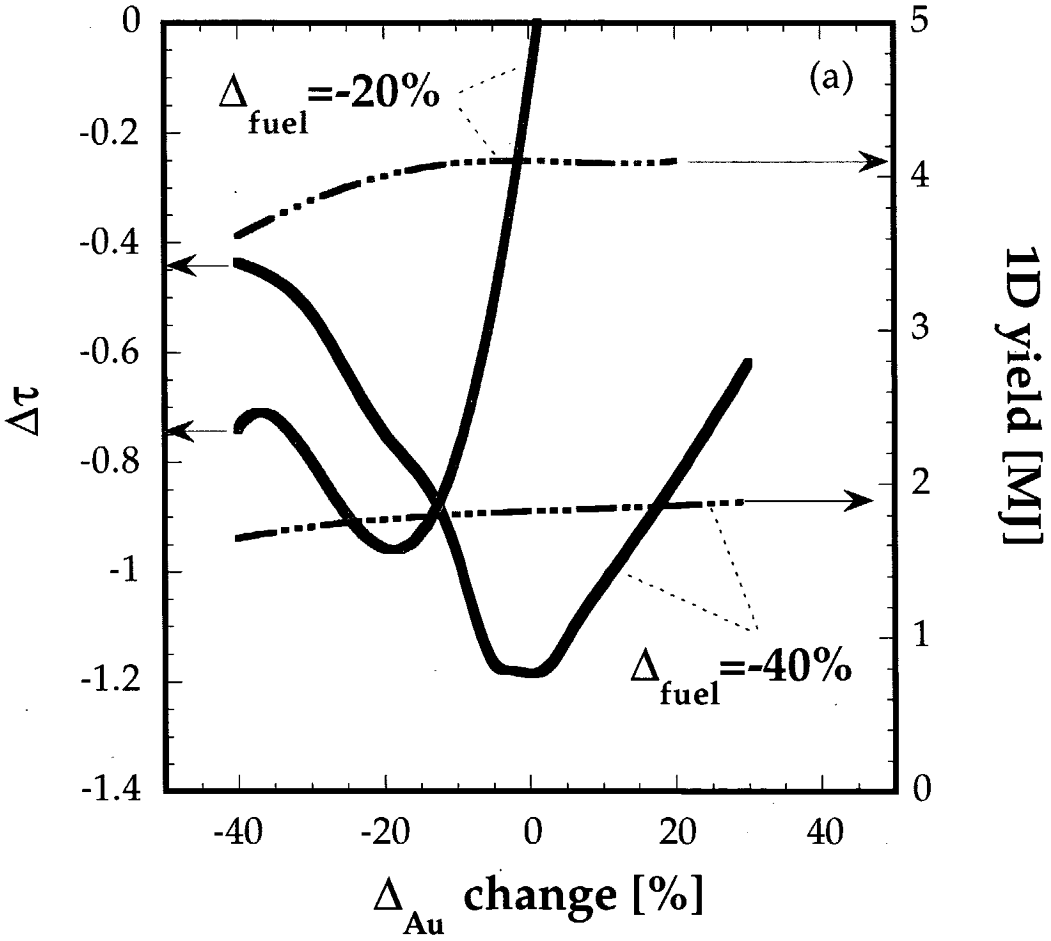

(a)
Δ_{fuel}=-20%
Δ_{fuel}=-40%
$\Delta\tau$
0
-0.2
-0.4
-0.6
-0.8
-1
-1.2
-1.4
1D yield [MJ]
5
4
3
2
1
0
-40
-20
0
20
40
Δ_{Au} change [%]

Fig. 4b

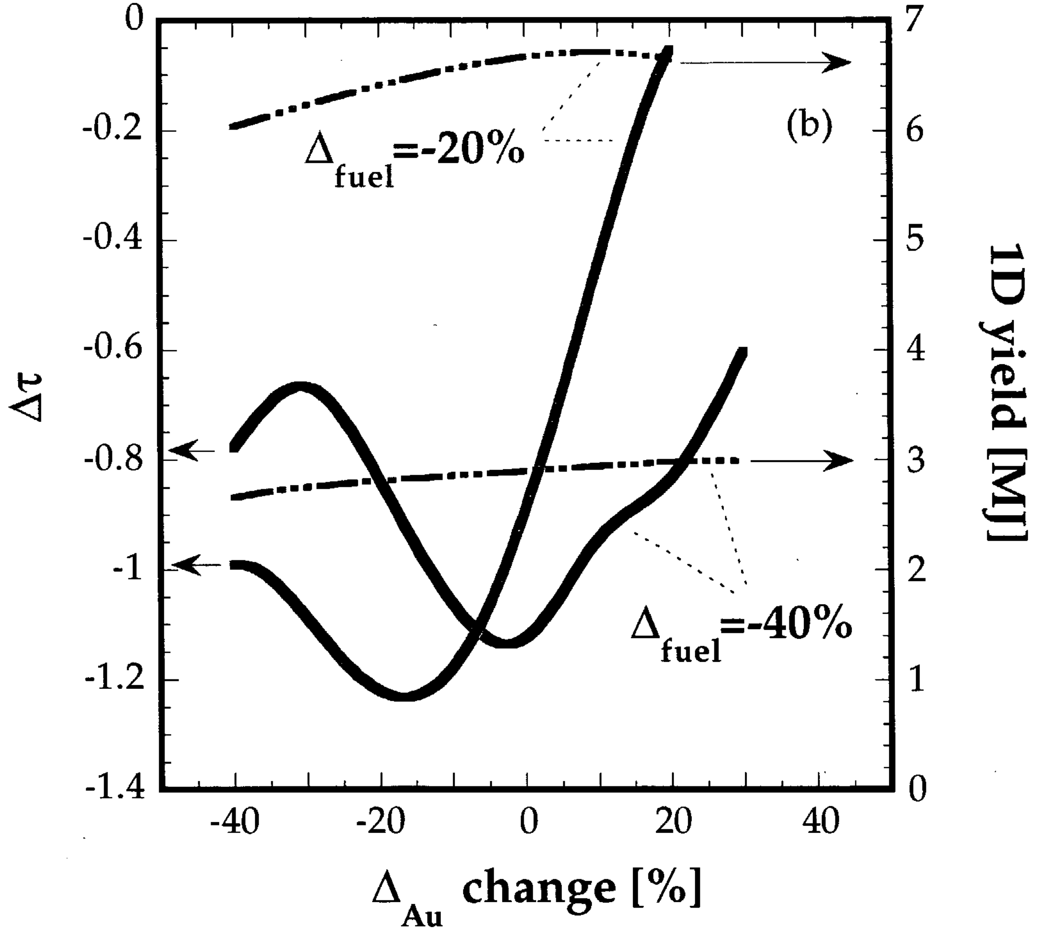
(b)
Δ_{fuel}=-20%
Δ_{fuel}=-40%
$\Delta\tau$
0
-0.2
-0.4
-0.6
-0.8
-1
-1.2
-1.4
1D yield [MJ]
7
6
5
4
3
2
1
0
-40
-20
0
20
40
Δ_{Au} change [%]

Fig. 5

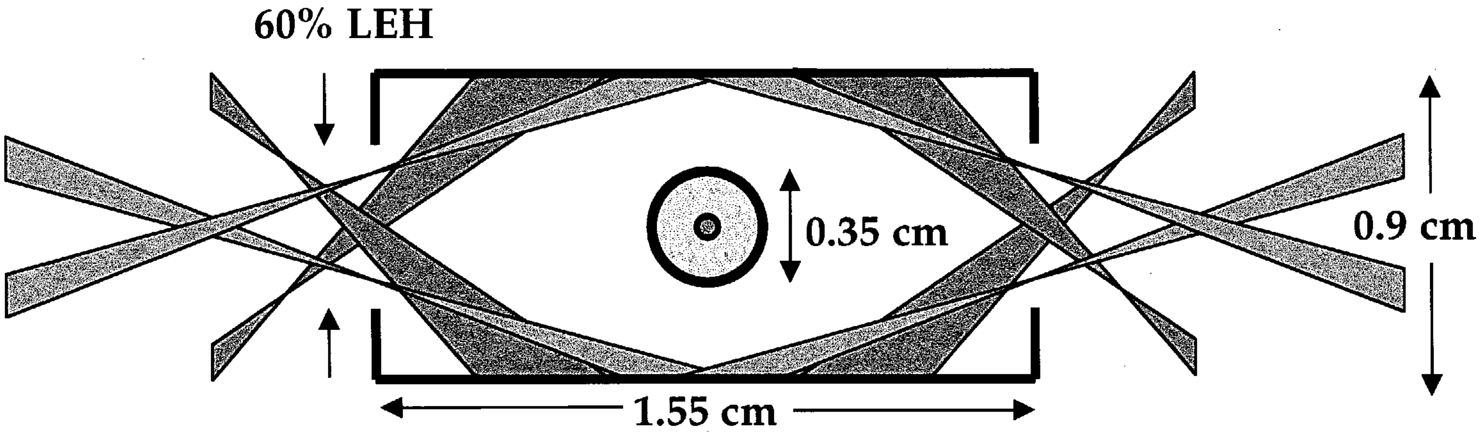
60% LEH
0.35 cm
0.9 cm
1.55 cm

Fig. 6

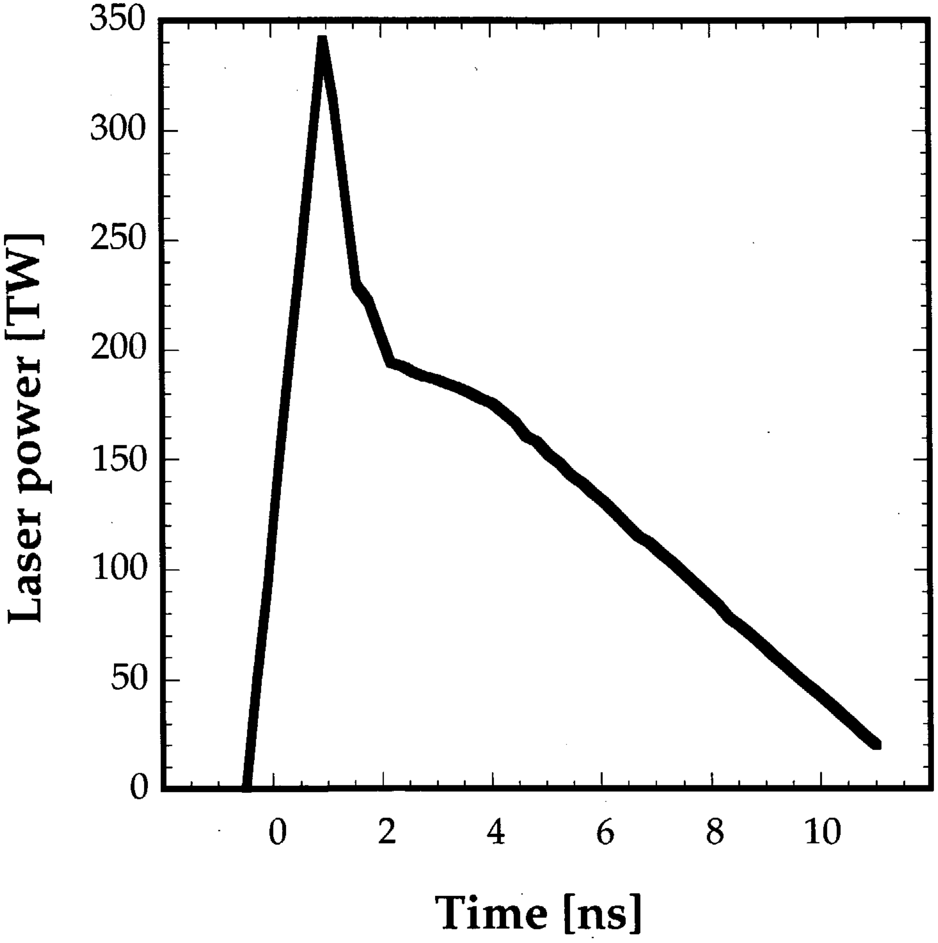

Fig. 7

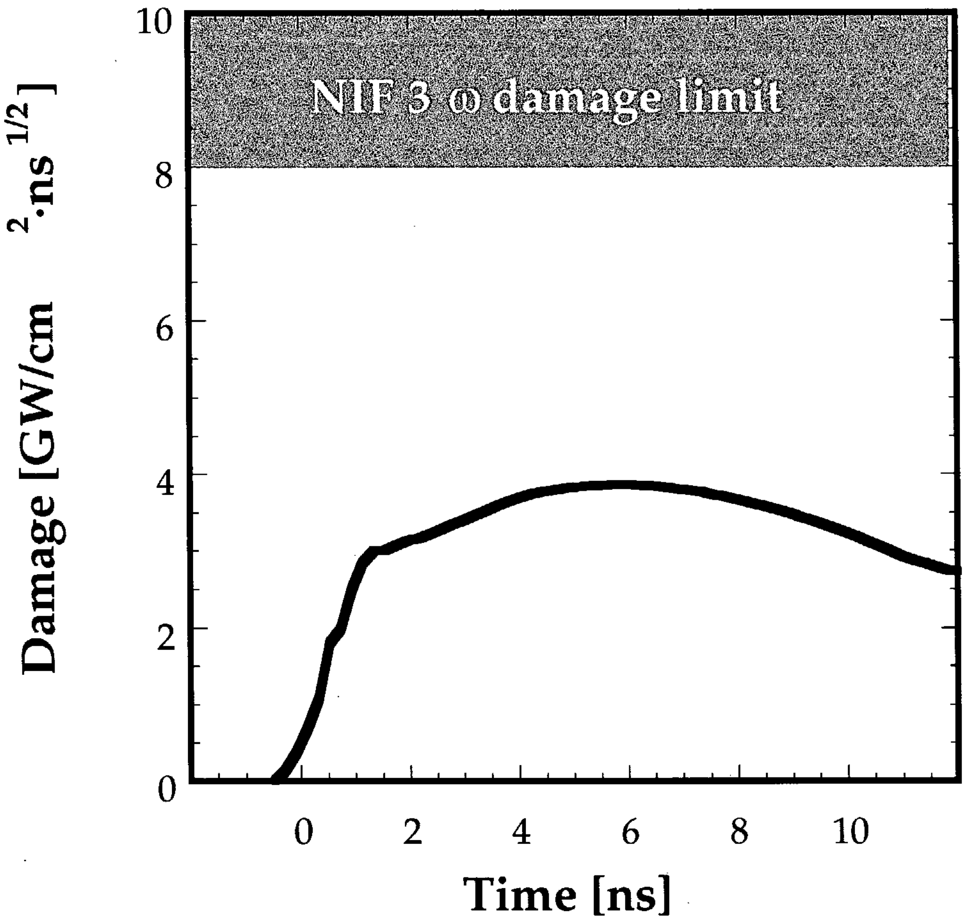

NIF 3 ω damage limit
10
8
6
4
2
0
Damage [GW/cm^2·ns$^{1/2}$]
0
2
4
6
8
10
Time [ns]

Fig. 8a

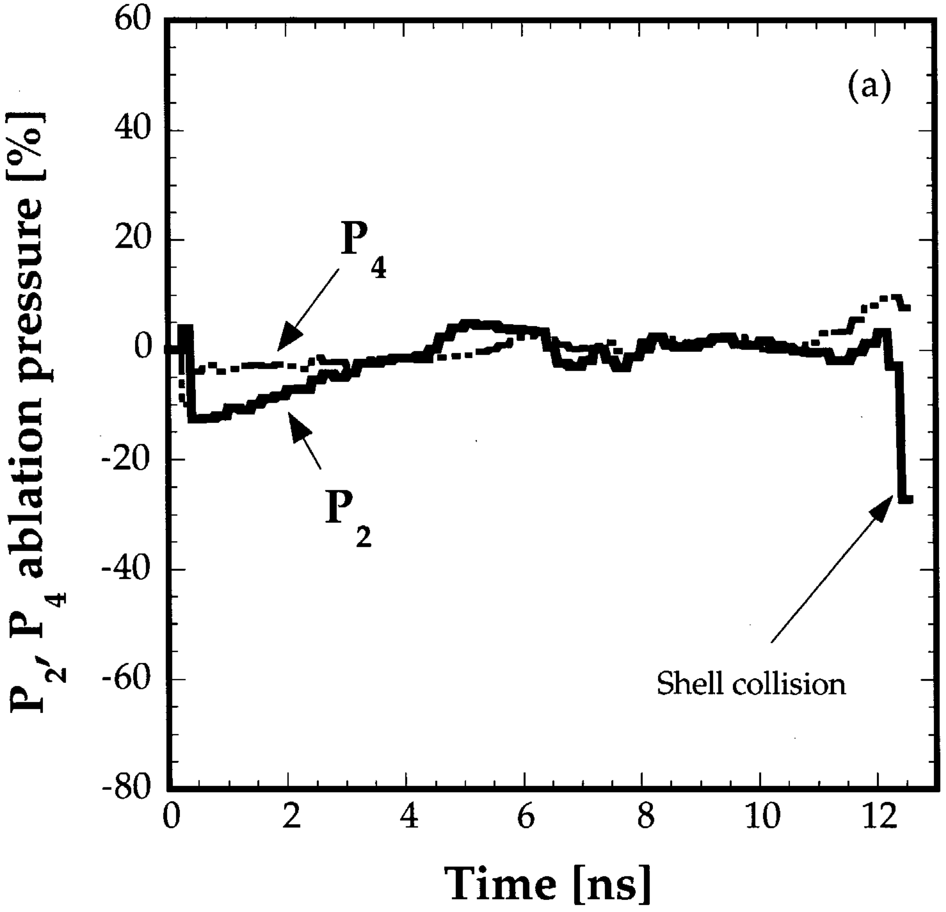
(a)
P_4
P_2
Shell collision
60
40
20
0
-20
-40
-60
-80
0
2
4
6
8
10
12
P_2, P_4 ablation pressure [%]
Time [ns]

Fig. 8b

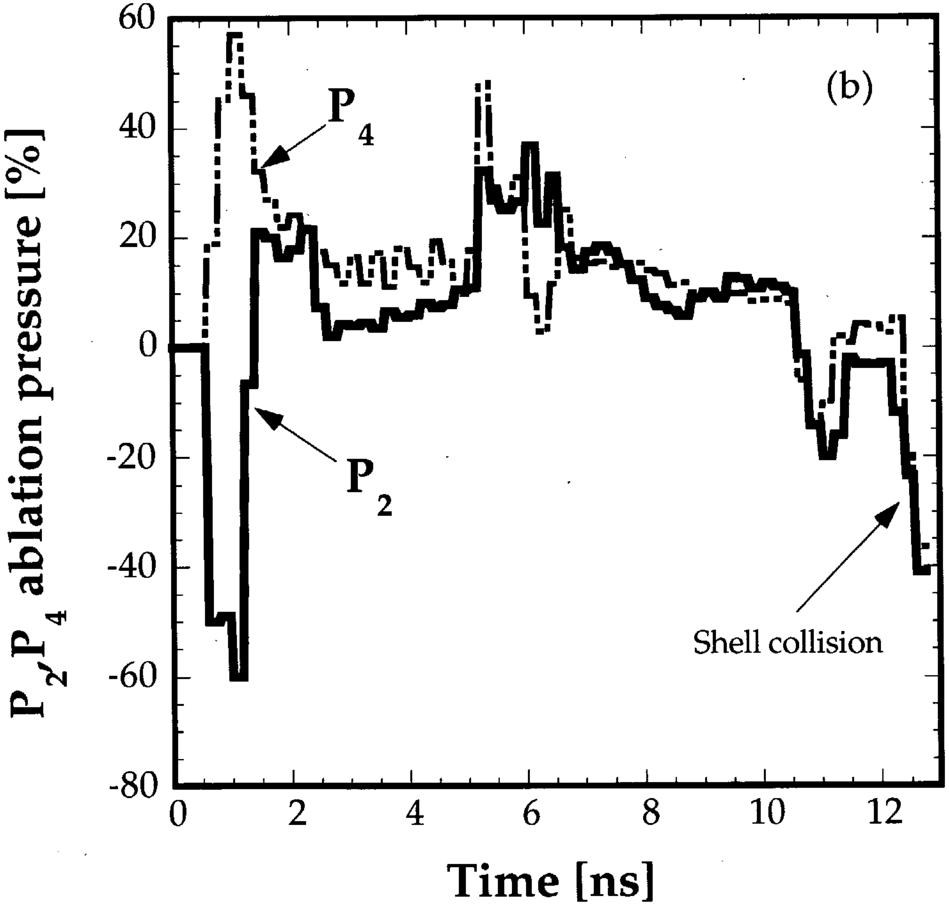
(b)
P4
P2
Shell collision
60
40
20
0
-20
-40
-60
-80
0
2
4
6
8
10
12
P2, P4 ablation pressure [%]
Time [ns]

Fig. 9a

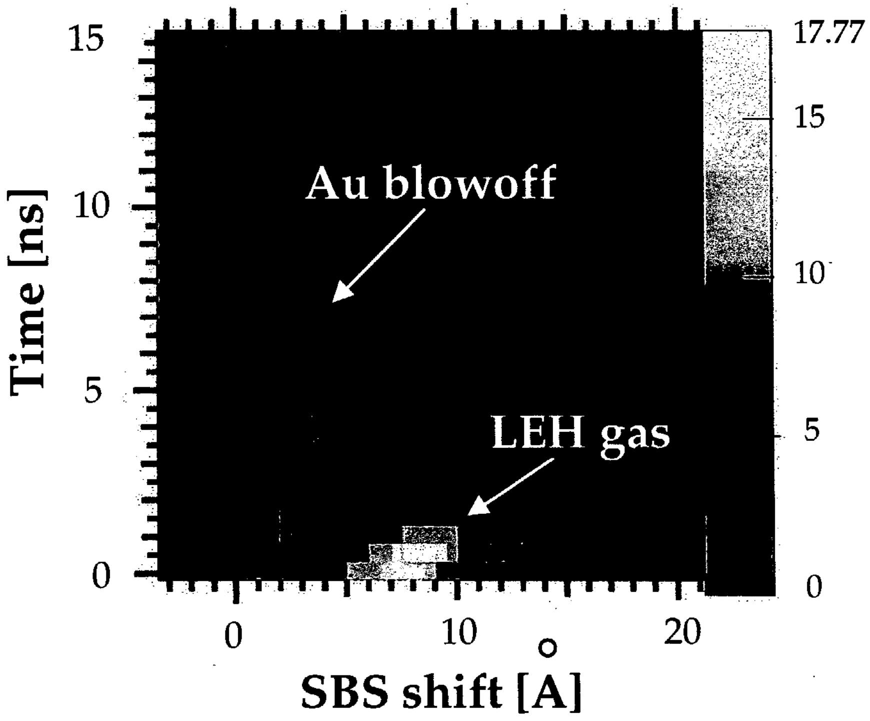
15
10
5
0
Time [ns]
0
10
20
SBS shift [Å]
Au blowoff
LEH gas
17.77
15
10
5
0

Fig. 9b

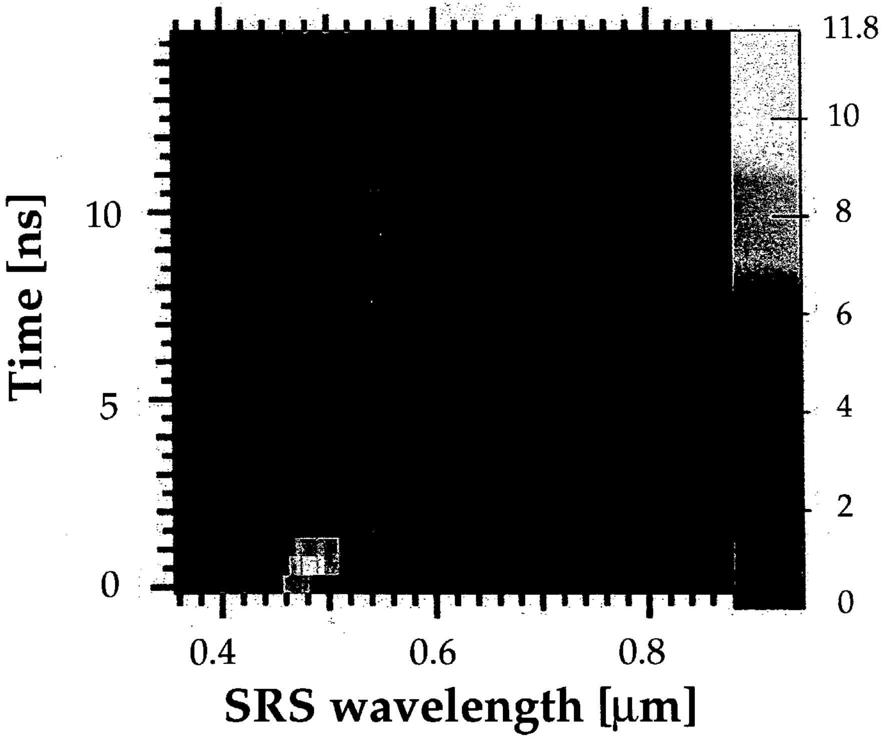

Fig. 10

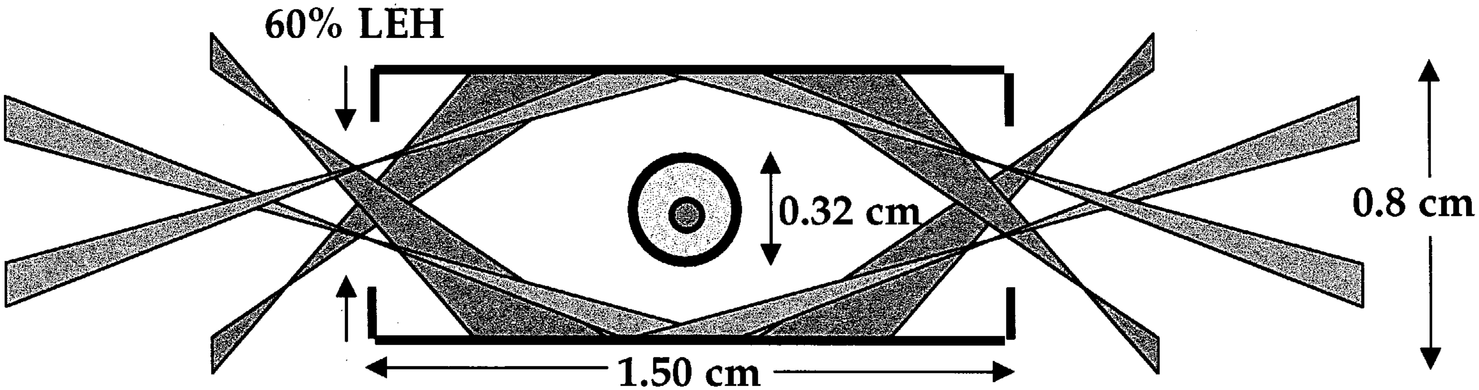
60% LEH
0.32 cm
0.8 cm
1.50 cm

Fig. 11

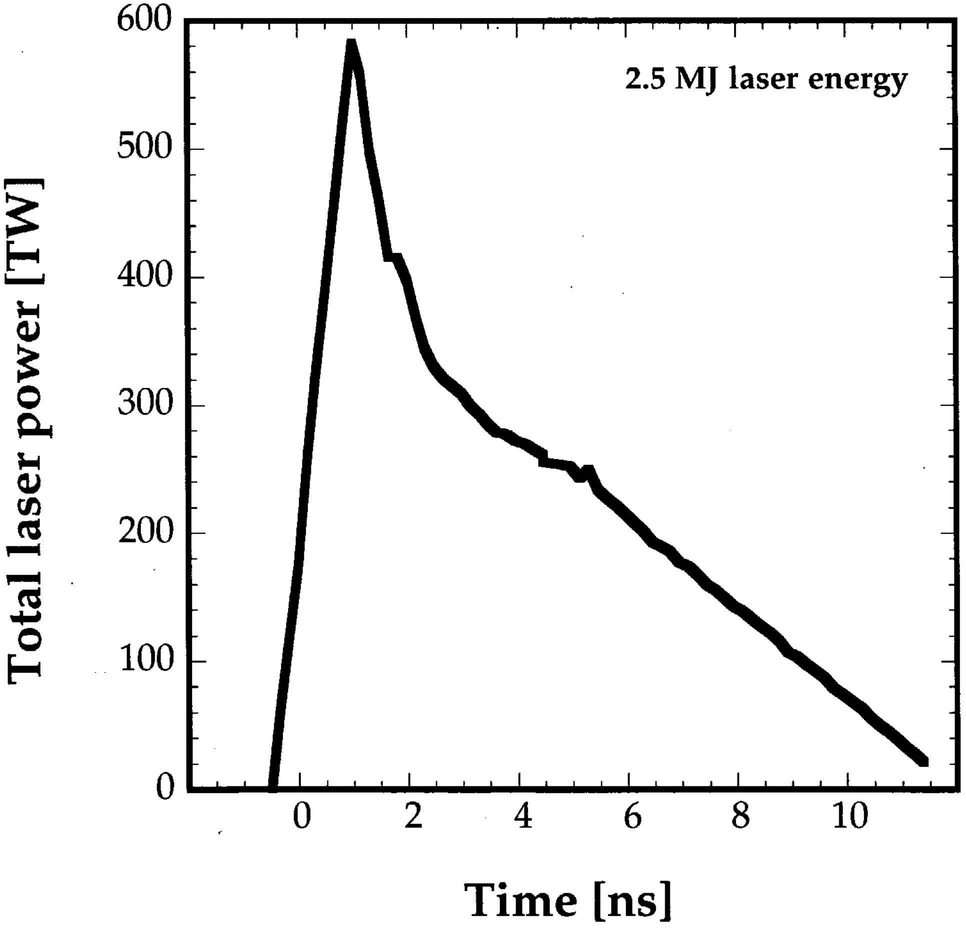
2.5 MJ laser energy
Total laser power [TW]
600
500
400
300
200
100
0
0
2
4
6
8
10
Time [ns]

Fig. 12

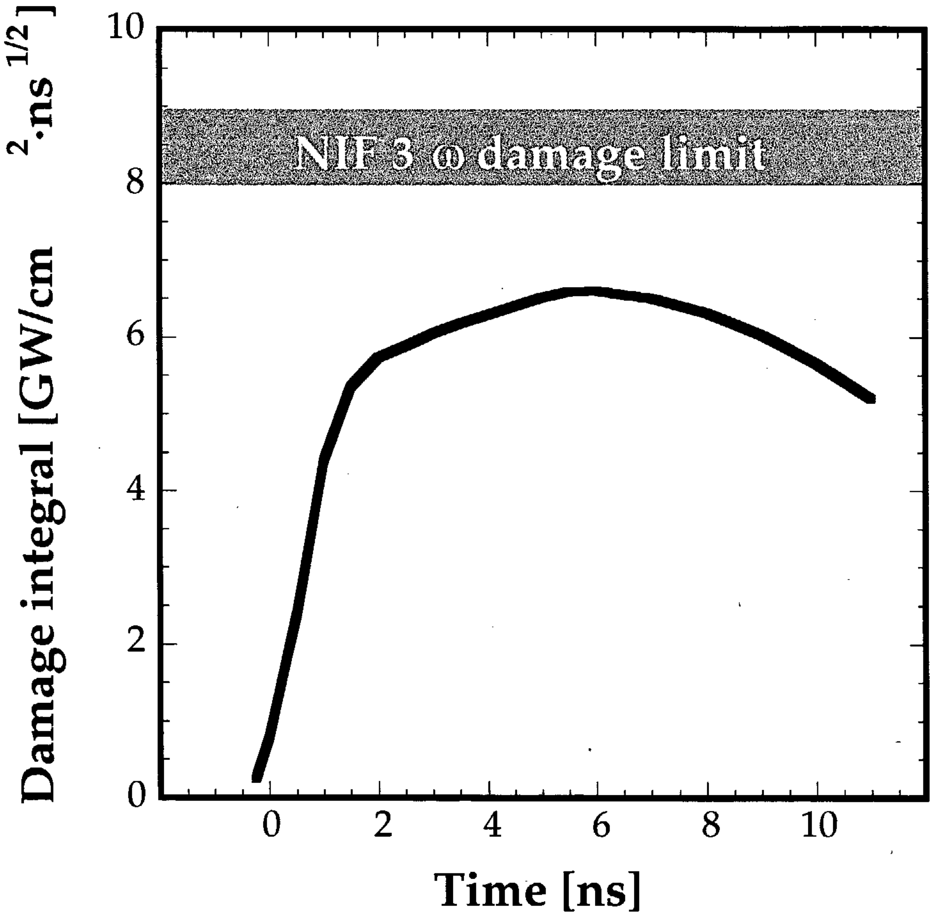

10
8
6
4
2
0
NIF 3 ω damage limit
0
2
4
6
8
10
Time [ns]
Damage integral [GW/cm^2·ns$^{1/2}$]

Fig. 13a

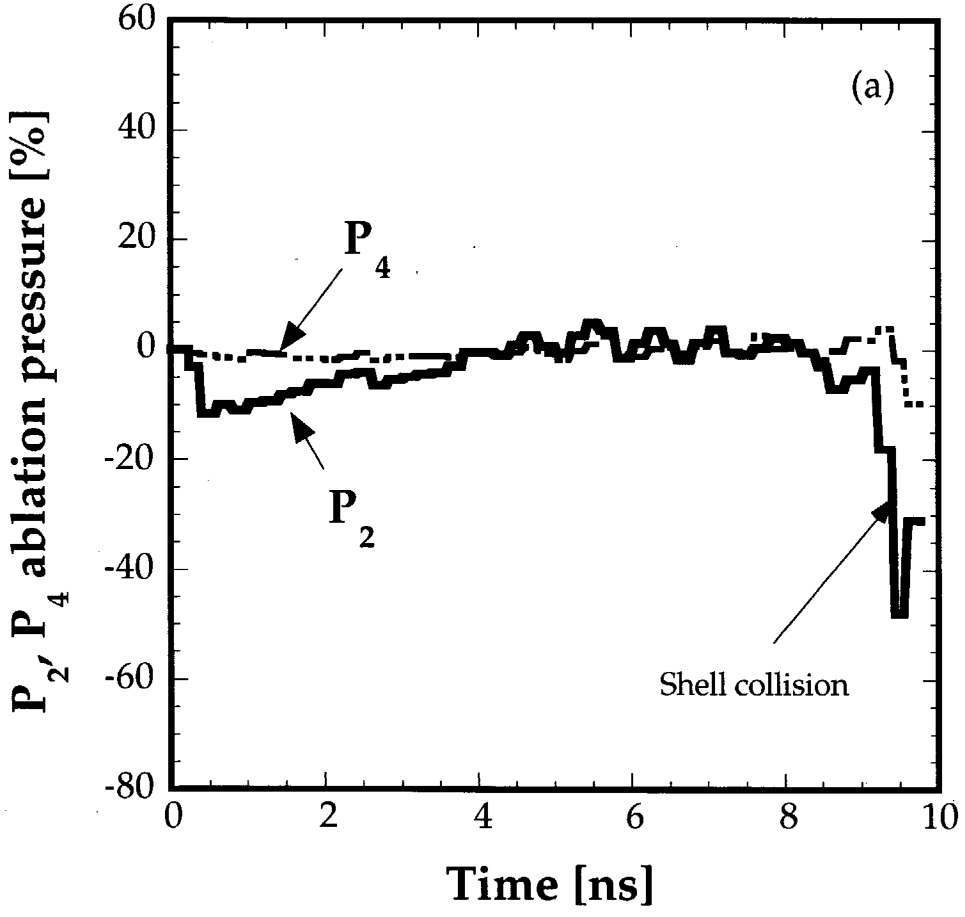

(a)
P_4
P_2
Shell collision
P_2, P_4 ablation pressure [%]
Time [ns]
60
40
20
0
-20
-40
-60
-80
0
2
4
6
8
10

Fig. 13b

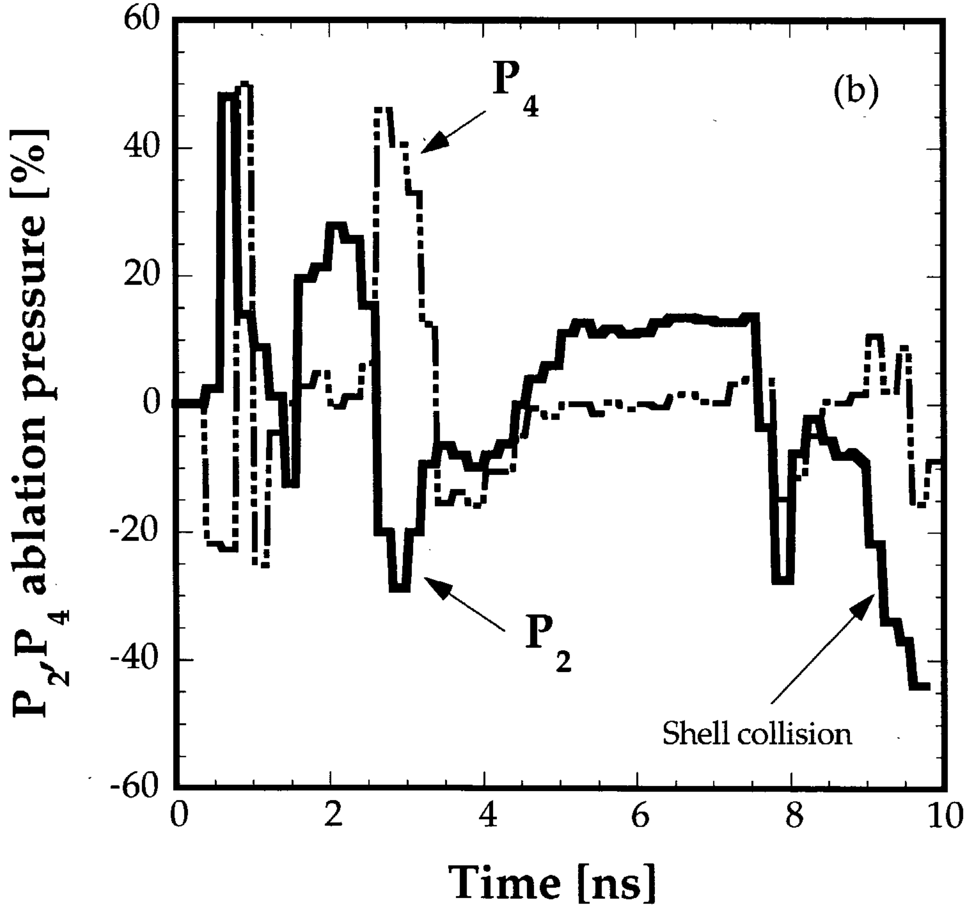

60
40
20
0
-20
-40
-60
0
2
4
6
8
10
P$_2$,P$_4$ ablation pressure [%]
Time [ns]
P$_4$
P$_2$
(b)
Shell collision

Fig. 14a

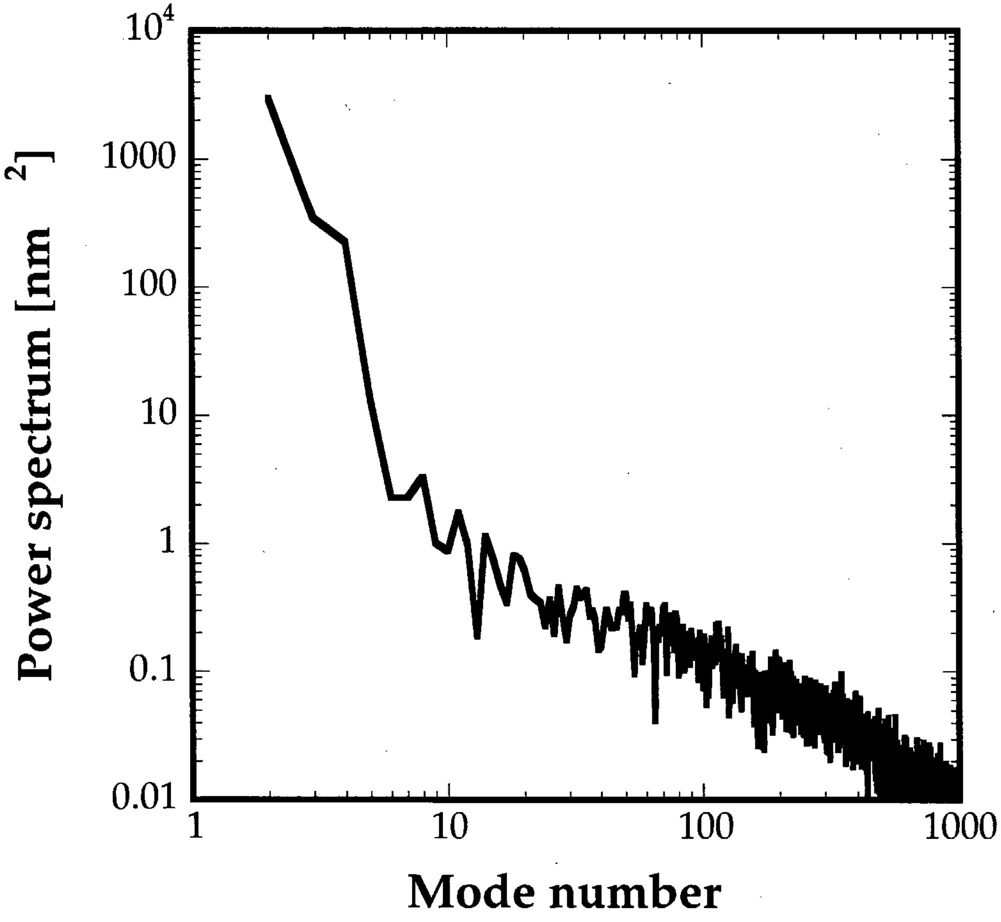

Power spectrum [nm 2]
10^4
1000
100
10
1
0.1
0.01
1
10
100
1000
Mode number

Fig. 14b

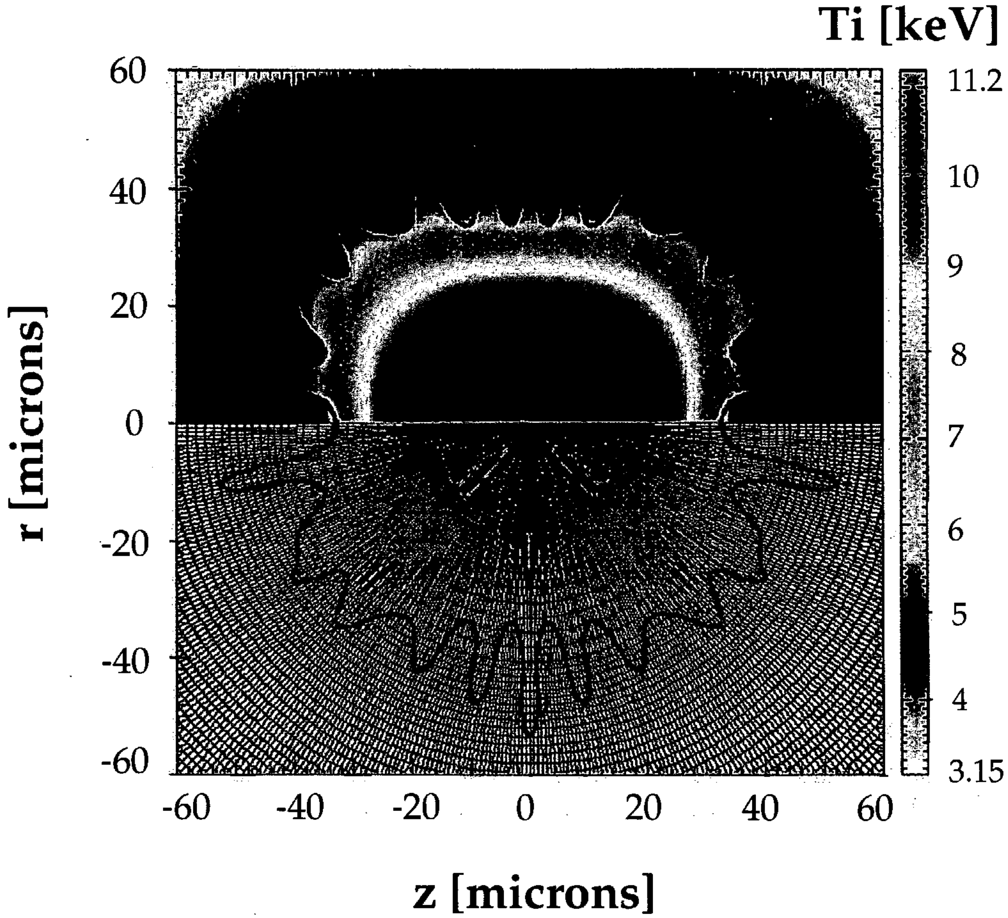
Ti [keV]
11.2
10
9
8
7
6
5
4
3.15
60
40
20
0
-20
-40
-60
r [microns]
-60
-40
-20
0
20
40
60
z [microns]

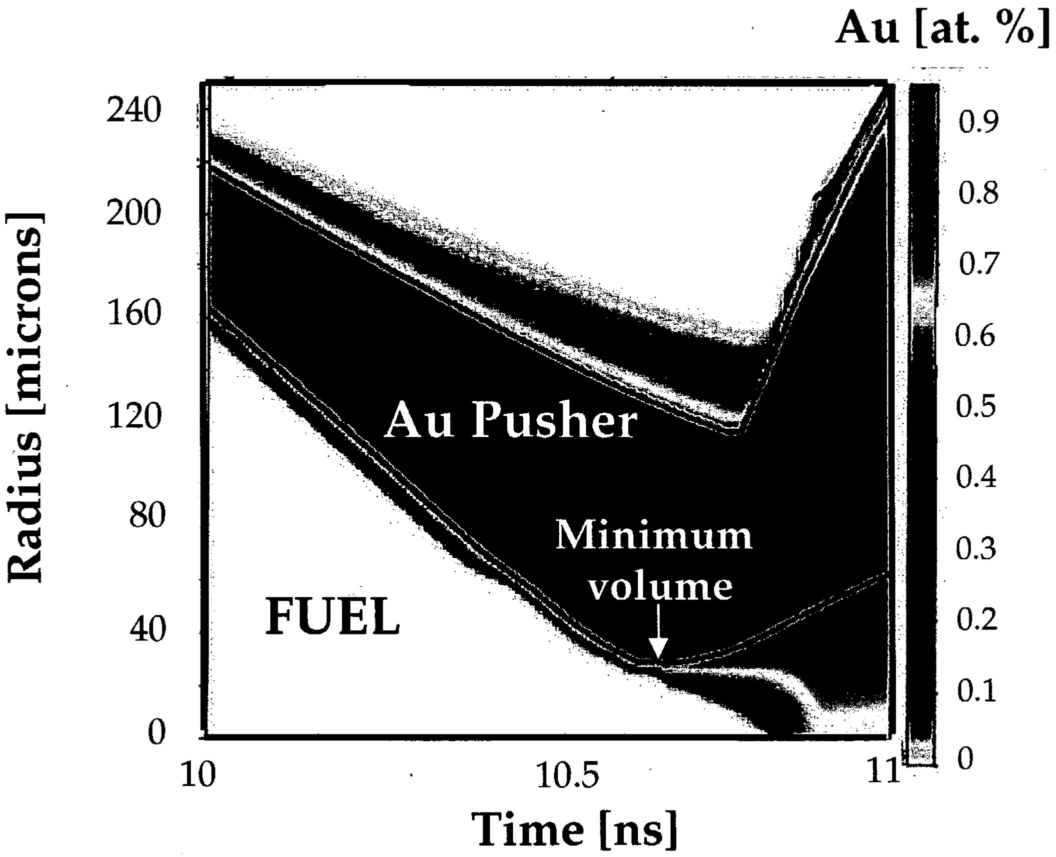
Au [at. %]
0.9
0.8
0.7
0.6
0.5
0.4
0.3
0.2
0.1
0
Radius [microns]
240
200
160
120
80
40
0
Au Pusher
Minimum volume
FUEL
10
10.5
11
Time [ns]

Fig. 16

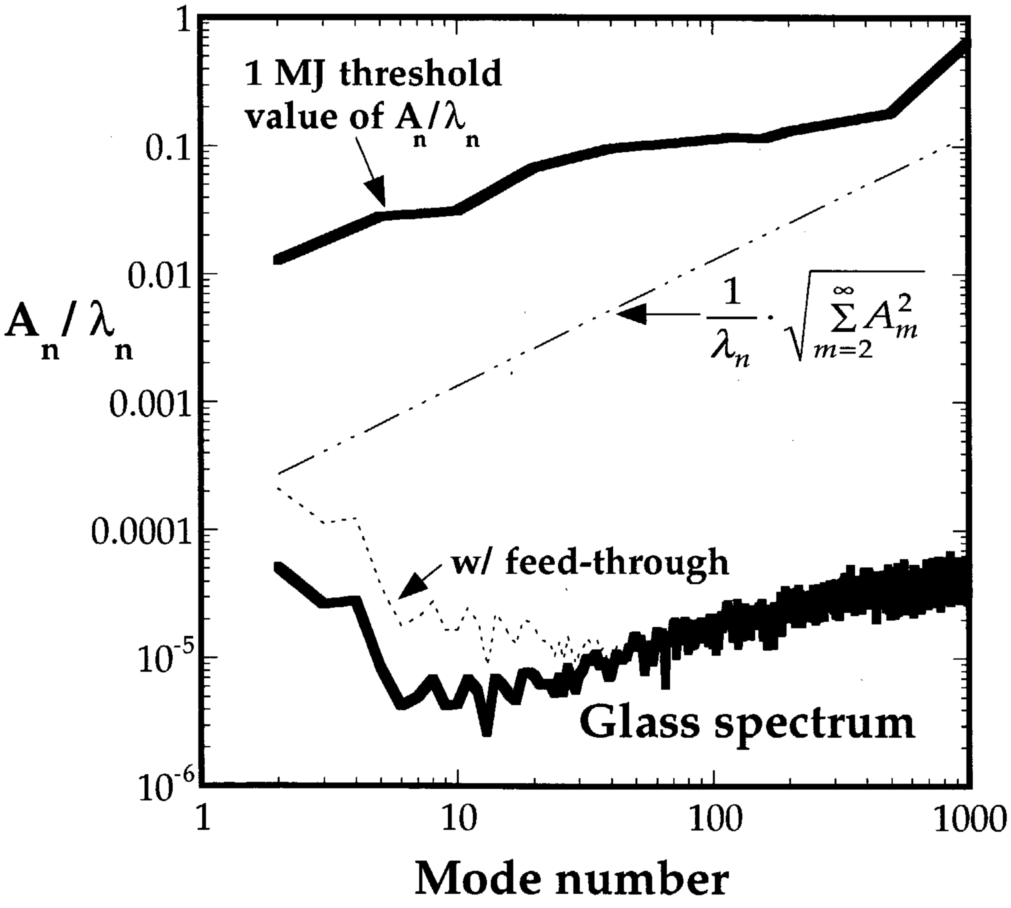
1 MJ threshold value of A_n/λ_n
$\frac{1}{\lambda_n} \cdot \sqrt{\sum_{m=2}^{\infty} A_m^2}$
w/ feed-through
Glass spectrum
A_n / λ_n
1
0.1
0.01
0.001
0.0001
10^{-5}
10^{-6}
1
10
100
1000
Mode number

Fig. 17

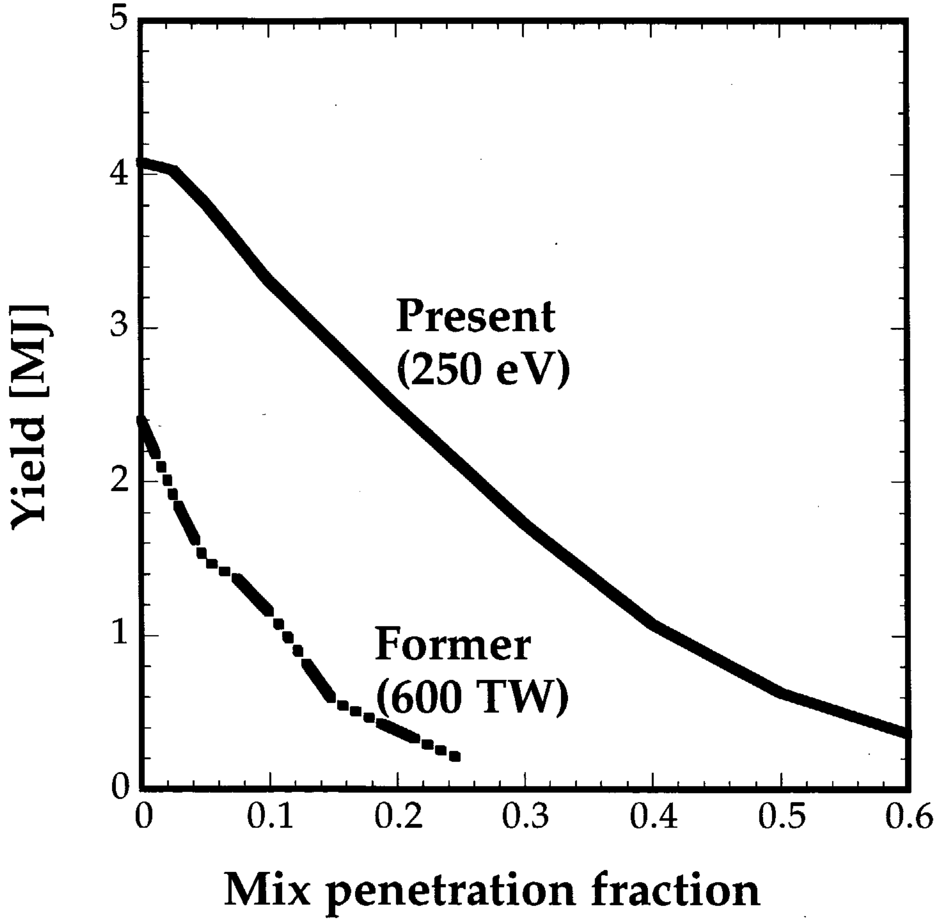

Yield [MJ]
Mix penetration fraction
0
1
2
3
4
5
0
0.1
0.2
0.3
0.4
0.5
0.6
Present
(250 eV)
Former
(600 TW)

Fig. 18

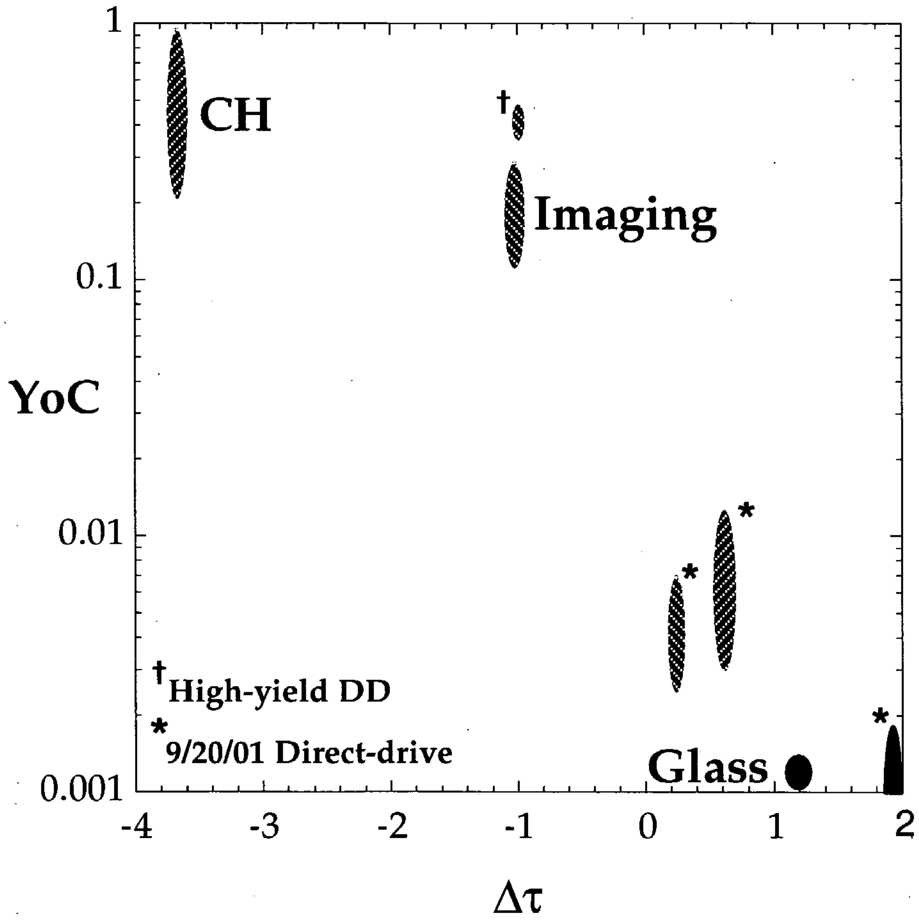
1
0.1
0.01
0.001
YoC
CH
†
Imaging
*
*
*
Glass
†High-yield DD
*9/20/01 Direct-drive
-4
-3
-2
-1
0
1
2
Δτ

Fig. 19

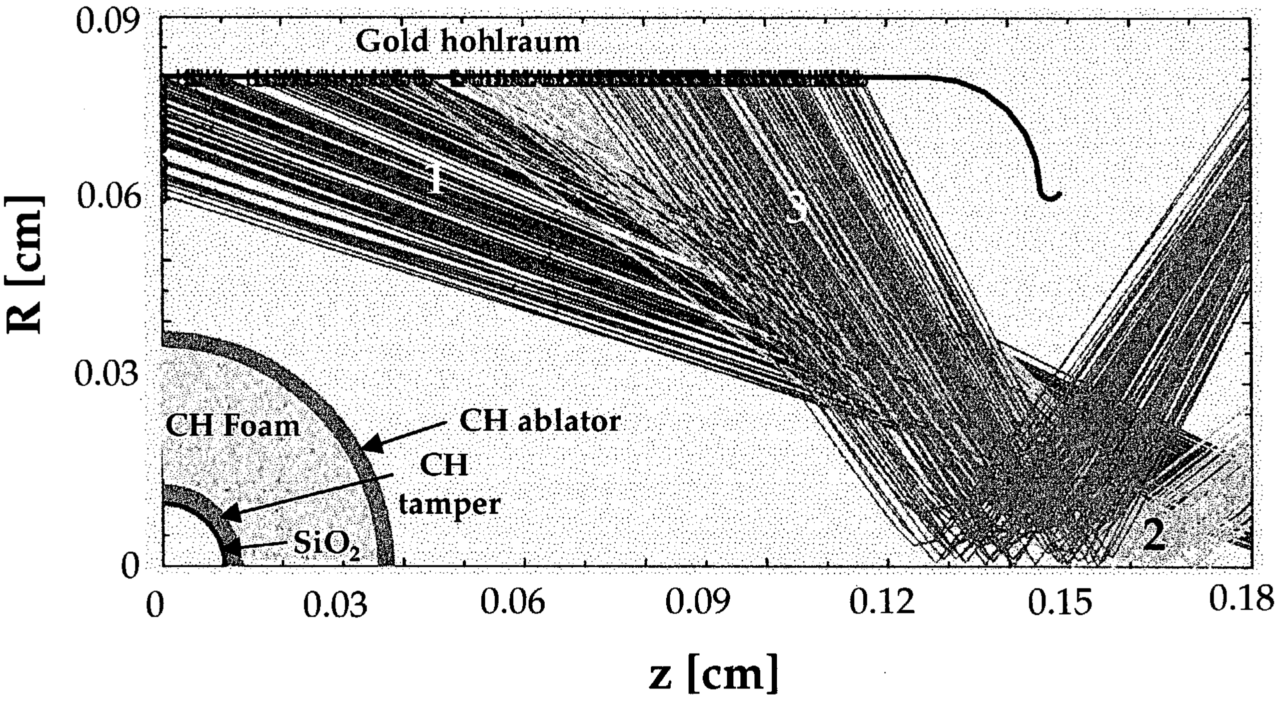
Gold hohlraum
1
3
2
CH Foam
CH ablator
CH tamper
SiO_2
R [cm]
0.09
0.06
0.03
0
z [cm]
0
0.03
0.06
0.09
0.12
0.15
0.18

Fig. 20

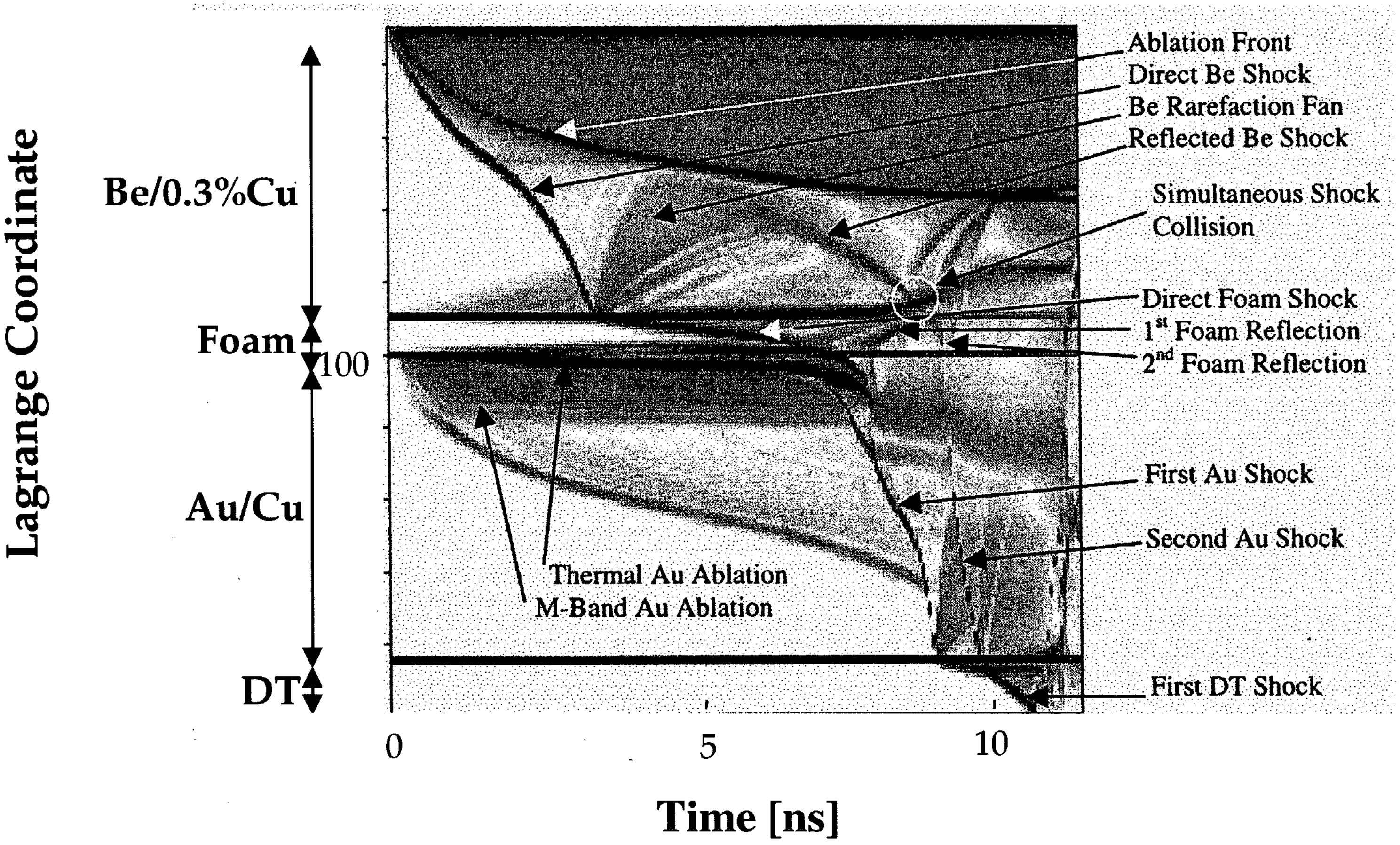
Lagrange Coordinate
Be/0.3%Cu
Foam
100
Au/Cu
DT
Ablation Front
Direct Be Shock
Be Rarefaction Fan
Reflected Be Shock
Simultaneous Shock Collision
Direct Foam Shock
1st Foam Reflection
2nd Foam Reflection
First Au Shock
Second Au Shock
Thermal Au Ablation
M-Band Au Ablation
First DT Shock
0
5
10
Time [ns]